Numerical analysis of the influence of the damping rings dimensions on interrupted dynamic tension experiment results.

González-Lezcano, R.A.[(1)]; del Río, J.M.[(2)]

[(1)] *Corresponding author. San Pablo CEU University, Architecture and Design Department Montepríncipe Campus, 28668 Boadilla del Monte, Madrid (Spain). rgonzalezcano@ceu.es*

[(2)] *San Pablo CEU University, Architecture and Design Department Montepríncipe Campus, 28668 Boadilla del Monte, Madrid (Spain). jmdrc.eps@ceu.es*

Abstract

This paper discusses the influence of the dimensions of the damping rings used for interrupting a dynamic tension experiment on the results of a modified Split Hopkinson Tension Bar (SHTB). The damping rings enclosed in an external fixture which modifies the classical SHTB play a significant role in buffering the dynamic tension experiments before the specimen reaches its failure strength. Finite-element (FE) simulations of high-strain-rate tension experiments are accomplished on Aluminum 7017-T73 alloy specimens when varying the thickness or the cross-sectional area of the damping rings. FE analyses described herein are applied to simulate the effects of the variation of the damping rings dimensions to provide a reference for improvement of a modified SHTB experimental apparatus and guidance for future studies in which optimum dimensions for the damping rings can be studied. In view of this research, it can be concluded that the thickness of the damping rings is a factor that can resolutely influence the interrupted dynamic tension experiment results whilst their cross-sectional area can be excluded as a factor influencing the results of the modified SHTB experiments.

Keywords— Dynamic tension experiment, High strain rate testing, damping rings, stress-strain curve, Finite Element Method, Split Hopkinson Tension Bar.

1. Introduction

In recent years various experimental techniques have been extensively employed in characterizing the high-strain rate behaviour of engineering materials. Scientists and engineers have widely used the Split Hopkinson Bar technique to study such dynamic behaviour under high rate loading. The Split Hopkinson Bar, which may be used in compression (SHCB), tension (SHTB) and torsion (SHToB) testing, seems to be the most widespread method for material characterization at high strain rates because a well-defined stress and strain state is feasible [1–7] and material properties at high tensile stress and strain rates can consequently be obtained. SHTB is commonly used for testing different materials at strain rates in the range between 200 and 1,500 s^{-1}.

The working principle of SHTB has been well documented in literature [8], [9]. The classical apparatus consists of two elastic bars called the incident and the transmission bars between which a specimen of the material being tested is sandwiched. An elastic striker bar imparts a uniaxial stress pulse towards the incident bar and a tensile wave is therefore produced. After the impact, this incident wave travels along the input bar towards the specimen where it is partly reflected back into the input bar while the other part is transmitted along the output bar. The

strain histories of the incident, reflected and transmitted waves are recorded by means of strain gauges suitably mounted on both bars. By adjusting the impact speed of the impactor, the strain rate can be varied.

The primary assumptions of the SHTB analysis are uniform deformation of the specimen and the absence of stresses in transverse direction [10]. Other assumptions include a constant strain rate while testing and quick equilibration of stresses in the specimen. According to the one-dimensional (1D) wave theory and the assumption of a uniaxial and homogeneous stress and strain in the specimen, the stress, strain and strain rate can be therefore calculated [11]. The 1D elastic wave theory is valid only if wave dispersion due to three-dimensional effects (radial inertia of the bars) can be neglected [12]. An extensive discussion and several critical remarks on high strain rate testing can be found in [13]. Consequently, the governing principles of SHTB include 1D stress wave propagation equation, uniaxial stress and strain relations, in addition to the conservation of momentum [14], [15].

Dynamic loads are not instantaneously propagated inside the impacted bodies. On the contrary, the propagation of these waves from the impact area to the entire specimen is a time-dependent variable [16]. The strain histories ε_i, ε_r and ε_t corresponding to respectively the incident, reflected and transmitted wave are measured at well chosen points on the Hopkinson bars [17].

The feasibility of a FE modified SHTB model for dynamic experiments is presented in this paper. In addition, the influence of the dimensions of the damping rings inserted in a modified SHTB on the interrupted dynamic tension experiment results is discussed below. The damping rings enclosed in an external fixture which modifies the classical SHTB play a significant role in buffering the dynamic tension experiments before the specimen reaches its failure strength.

The SHTB model considerably simplifies the stress wave theory and it simultaneously offers accurate and reproducible results. However, such model simplification involves several limitations which are discussed below. The parameters of interest in SHTB model are developed considering an elastic behaviour of the bars. In relation to the specimen, both elastic and plastic deformations are considered. The below-discussed necessary equations can be obtained through a single differential element, as described by Kaiser [18] and Swantek [19].

2. Materials description

The following materials and its mechanical properties detailed below are used both in experimental and FE simulation techniques.

The material of the specimen is an Aluminium 7017-T73 alloy. This alloy, one of the highest-strength aluminium alloys, contains zinc as the primary alloying element, magnesium which produces a marked improvement in precipitation hardening characteristics and chromium which provides an increase of the stress corrosion cracking resistance [20]. The alloy is treated with a T73 heat-treatment, which consists of a heat-treatment solution and artificial aging that leaves the alloy beyond the point of maximum strength and achieves the best stress corrosion resistance. Aluminium 7017 alloy is mainly used in armoured vehicles. This material is selected

because its mechanical behaviour has been found to be nearly independent upon the strain rate [21].

The table below (table 1) shows the mechanical properties of the Aluminum 7017-T73 alloy at high rates, the ones of the lead used for the damping rings and also the ones of the steel used in the Hopkinson bars and the interruption fixture at high strain rates.

	Aluminum 7017-T73	Lead	Steel
Poisson's ratio	0.3	0.45	0.3
Young's modulus (GPa)	63	10	202
Density (Kg/m^3)	2710	11000	7850
Yield strength (MPa)	507	33	
Ultimate tensile strength (UTS) (MPa)	563	42	
Ductility	0.12	0.6	

Table 1. Mechanical properties of the materials used both in experimental and FE simulation techniques.

3. Theoretical considerations.

The 1D stress wave propagation equation can be derived from Hooke's law. The equilibrium condition for a differential element of the Hopkinson bar is shown below. The stress wave propagation is taken along the longitudinal axis of the bar, i.e., x-axis, as shown in fig. 1. Rightward displacement along the x-axis (i.e. elongation) is considered positive and leftward displacement (shortening) along the same axis is considered negative. In addition, tensile stress is considered positive and compressive stress is considered negative.
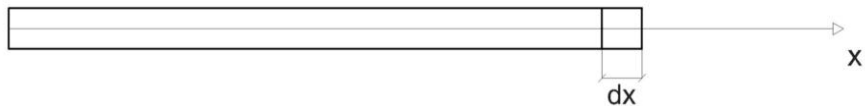

Figure 1. Differential element of the bar.
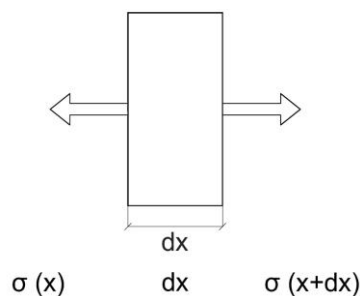

σ (x)   dx   σ (x+dx)

Figure 2. Normal stress equilibrium condition in a differential element of the bar.

The resultant differential force obtained when setting up the equilibrium condition of the tension forces acting on a differential element of the bar is

$$dF = A \cdot [\sigma(x+dx) - \sigma(x)] = A \cdot [\sigma(x) + \delta\sigma/\delta x \cdot dx - \sigma(x)] = A \cdot \delta\sigma/\delta x \cdot dx \qquad (1)$$

where A is the cross-sectional area of the bar and σ is the uniaxial stress. Moreover, using Newton's law and replacing mass by the product of volume and density, the resultant differential force can also be expressed as

$$dF = A \cdot \delta\sigma/\delta x \cdot dx = \rho \cdot A \cdot dx \cdot \delta^2 u/\delta t^2 \tag{2}$$

where ρ is the density of the material, t is time and u is the displacement of the differential element of the bar along the x-axis, i.e., the elongation of such differential element. For the apparatus to function as designed, the bars must constantly work under their yield strength. Consequently, according to Hooke's law,

$$\sigma = E \cdot \varepsilon \tag{3}$$

$$E \cdot \delta\varepsilon/\delta x = \rho \cdot \delta^2 u/\delta t^2 \tag{4}$$

where E is Young's modulus of the material and ε is the normal strain. Thereafter, elongation and strain can be related as

$$\varepsilon = \delta u/\delta x \tag{5}$$

and hence the 1D stress wave propagation equation reduces to

$$\delta^2 u/\delta t^2 = E / \rho \cdot \delta^2 u/\delta x^2 \tag{6}$$

where c is the speed of the stress wave (c = $\sqrt{E/\rho}$). Therefore the 1D stress wave propagation equation becomes

$$\delta^2 u/\delta t^2 = c^2 \cdot \delta^2 u/\delta x^2 \tag{7}$$

A relatively simple general solution of the 1D stress wave propagation equation may be found:

$$u(x,t) = F(x - c{\cdot}t) + G(x + c{\cdot}t) \tag{8}$$

Consequently, the following expressions can be used considering 1D stress wave propagation in the rightward direction along the x-axis:

$$u(x,t) = F(x - c{\cdot}t) \tag{9}$$

$$\varepsilon = \delta u/\delta x = F'(x - c{\cdot}t) \tag{10}$$

$$v = \delta u/\delta t = - c \cdot F'(x - c{\cdot}t) \tag{11}$$

And hence stress and velocity (i.e. displacement over time) can get related as follows:

$$\sigma = - \rho \cdot c \cdot v \tag{12}$$

where ρ·c is the proportionality constant known as mechanical impedance of the material. In the particular case of wave propagation in the leftward direction along the x-axis, the following expressions can be used:

$$u(x,t) = F(x + c{\cdot}t) \tag{13}$$

$$\varepsilon = F'(x + c{\cdot}t) \tag{14}$$

$$v = c \cdot F'(x + c{\cdot}t) \tag{15}$$

$$\sigma = \rho \cdot c \cdot v \tag{16}$$

The solution obtained is linear and, therefore, the superposition principle applies. Consequently, if two pulses coincide in a determined instant, the solution can be obtained adding the solutions of each separate pulse.
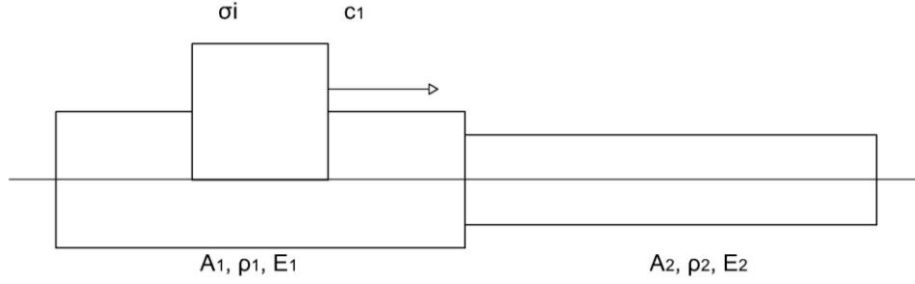

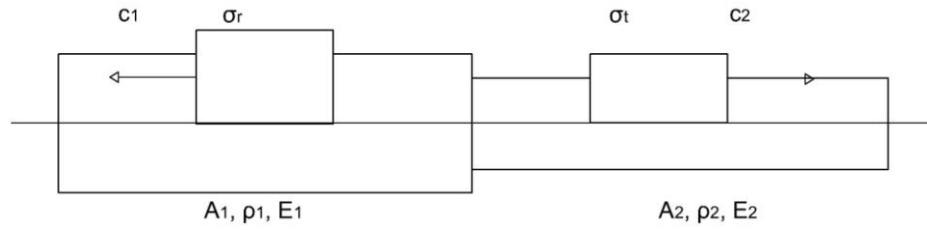Figure 3. Incident wave when both cross-sectional area and transmission medium are changed.

Figure 4. Reflected and transmitted waves when both cross-sectional area and transmission medium are changed.

Equations (17) and (18) show the equilibrium conditions for forces and velocities when both cross-sectional area and transmission medium are changed as shown in figure 3 and figure 4. Different values of the material's density and the material's Young's modulus are used when the transmission medium is changed.

$$A_1 \cdot (\sigma_i + \sigma_r) = A_2 \cdot \sigma_t \tag{17}$$

$$v_i + v_r = v_t \tag{18}$$

where σ_i, σ_r, and σ_t are the incident, reflected, and transmitted stresses, respectively, and v_i, v_r, and v_t are the incident, reflected, and transmitted velocities, respectively. Using $v = \sigma / \rho \cdot c$, the following equalities can be obtained from (17) and (18):

$$\sigma_t = [(2 \cdot A_1 \cdot \rho_2 \cdot c_2) / (A_1 \cdot \rho_1 \cdot c_1 + A_2 \cdot \rho_2 \cdot c_2)] \cdot \sigma_i \tag{19}$$

$$\sigma_r = [(A_2 \cdot \rho_2 \cdot c_2 - A_1 \cdot \rho_1 \cdot c_1) / (A_1 \cdot \rho_1 \cdot c_1 + A_2 \cdot \rho_2 \cdot c_2)] \cdot \sigma_i \tag{20}$$

The calculation of σ_t from σ_i is the starting point to compute the impact on the incident bar. The strain at the end of each bar (i.e., ε_1 at the end of the incident bar and ε_2 at the end of the transmission bar) can be computed as follows:

$$\varepsilon_1(t) = \varepsilon_i(t - T_1) + \varepsilon_r(t + T_1) = \varepsilon_{i1}(t) + \varepsilon_{r1}(t) \tag{21}$$

where ε_i is the strain caused by the incident pulse and ε_r the strain caused by the reflected strain. T_1 is the time elapsed while the wave moves from the strain gauge to the specimen and vice versa.

$$\varepsilon_2(t) = \varepsilon_t(t + T_2) = \varepsilon_{t2}(t) \tag{22}$$

where ε_t is the strain caused by the transmitted pulse and T_2 is the time elapsed while the wave moves from the end of the transmission bar and the strain gauge.

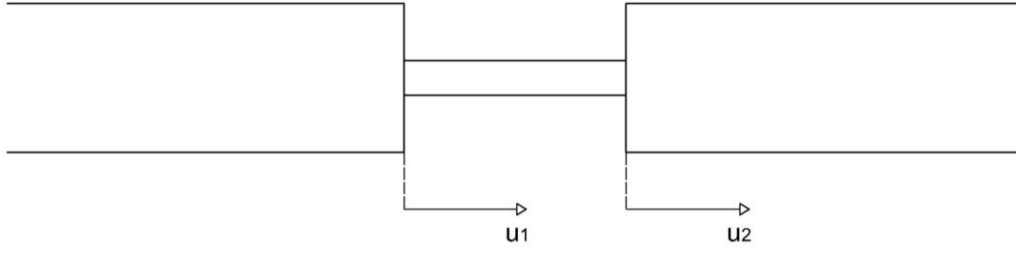Figure 5 shows the displacements of each end of the specimen.

Figure 5. Displacements of each end of the specimen.

Using subscripts 1 and 2 to refer to the two specimen ends (fig. 5), the velocity of end 2 is given by:

$$v_2 = - c \cdot \varepsilon_2 \tag{23}$$

Since at end 1 two waves (i.e. incident and reflected) are found, velocities can be added using equations (27) and (31).

$$v_1 = v_{1i} + v_{1r} = - c \cdot \varepsilon_{i\,1} + c \cdot \varepsilon_{r\,1} = - c \cdot [\varepsilon_{i\,1} - \varepsilon_{r\,1}] \tag{24}$$

Therefore, displacements can be obtained by integration.

$$u_1 = \int v_1 \cdot dt = - \int c \cdot [\varepsilon_{i\,1} - \varepsilon_{r\,1}] \cdot dt \tag{25}$$
$$u_2 = \int v_2 (t) \cdot dt = - \int c \cdot \varepsilon_2 \cdot dt \tag{26}$$

The mean strain can be computed from the displacements on each end of the specimen.

$$\varepsilon_p = (u_1 - u_2) / L = - c / L \cdot \int [\varepsilon_{i\,1} - \varepsilon_{r\,1} - \varepsilon_{2\,t}] \cdot dt \tag{27}$$

where L is the specimen length, u_1 is the displacement of the left end and u_2 is the displacement of the right end, as shown in fig. 5. When finding the derivative of (27), the mean strain rate of the specimen can be obtained.

$$d\varepsilon_p / dt = (v_1 - v_2) / L = - c / L \cdot [\varepsilon_{i\,1} - \varepsilon_{r\,1} - \varepsilon_{2\,t}] \tag{28}$$

Thereafter, the tension forces exerted on the bar ends can be computed, as shown in equation (29).

$$F_1 = A \cdot \sigma_1 = E \cdot A \cdot [\varepsilon_{i\,1} + \varepsilon_{r\,1}] \tag{29}$$
$$F_2 = A \cdot \sigma_2 = E \cdot A \cdot \varepsilon_{t\,2} \tag{30}$$

where A is the cross-sectional area of the bars and E is their Young's modulus. The mean uniaxial stress of the specimen can consequently be computed as:

$$\sigma_p = [F_1 + F_2] / (2 \cdot A_p) \tag{31}$$

Let the specimen have enough time to reach its equilibrium condition and therefore F_1 balances F_2. Therefore,

$$\varepsilon_i + \varepsilon_r = \varepsilon_t \tag{32}$$

The analysis is based on equilibration of forces acting on the incident and the transmission bars. Its validity is supported by previous studies [22].

The above-mentioned expressions may be simplified as follows:

$$\varepsilon_p = 2 \cdot c / L \cdot \int \varepsilon_{r1} \cdot dt \tag{33}$$
$$d\varepsilon_p / dt = 2 \cdot c / L \cdot \varepsilon_{r1} \tag{34}$$
$$\sigma_p = E \cdot A / A_p \cdot \varepsilon_{t2} \tag{35}$$

Hence the stress-strain curve can be obtained.

4. Experimental apparatus.

The SHTB apparatus as installed in the Universidad Carlos III de Madrid Engineering Laboratory shown in fig. 6 involves two steel bars called the incident and the transmission bars, and a specimen sandwiched between them made of the material being tested. The cylindrical bars are maufactured in a sole piece to facilitate the wave propagation study. Their dimensions are suitable for optimizing the experiments.

Figure 6. Split Hopkinson Tension Bar apparatus as installed in the Universidad Carlos III de Madrid Engineering Laboratory.

Two strain gauges mounted on the incident and transmission bars enable the stress waves to be measured. The information gathered by the strain gauges is sent to a data acquisition system that consists of a signal conditioner and an oscilloscope, where test data can be computed.
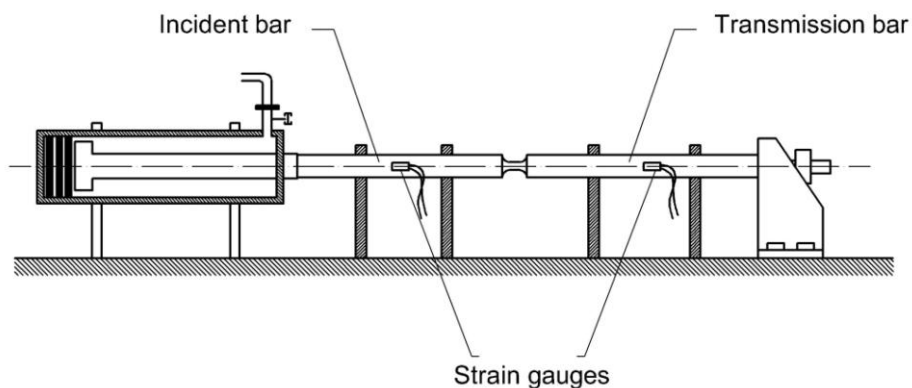
Figure 7. Strain gauges mounted on the SHTB apparatus.

The specimen ends are screwed into both the incident and transmission bar. The incident bar, which is longer than the transmission bar, is impacted by the steel projectile. The basic principle is to use a tubular projectile to impact the flange of the incident bar to generate compression waves which will be converted to tensile waves by the flange. The projectile is a hollow cylinder that is launched using a chamber with compressed gas with a maximum pressure of 8 bar. The optimum pressure in every test for the required impact can be chosen using a control valve. The stress pulse then travels through the input bar, the specimen and the output bar, and is recorded in order to obtain the stress-strain curve and draw conclusions about the specimen material behaviour using the 1D stress wave propagation theory [23]. The shape, duration and magnitude of this stress pulse determine the loading conditions of the specimen and the accuracy with which the experimentally generated data can be analysed.

The Finite Element Simulation of the projectile impact is conditioned by the SHTB experimental results. Damping the experiment offers the possibility to develop a study of the deformation process in detail. The emphasis is laid on the influence of the damping rings thickness on the specimen behaviour during the modified SHTB experiments. The distance between the strain gauges and the end of each bar is 500 mm and such distance is used when simulating the apparatus. The time elapsed while the stress wave travels from the gauge to the specimen is the quotient of the distance (d = 500mm) over the speed of the stress wave. The evolution in a material during dynamic experiments has been previously studied by interrupting the test at predetermined elongation values [24]. Therefore, the designed interruption fixture can control the elongation of the test specimen and produce a reliable predetermined strain on it.

The interruption mechanism is based on the use of two damping rings working as buffers which are enclosed in an external interruption fixture. They can absorb the impact energy by deforming plastically and therefore allowing a tensile stress distribution in the specimen. Otherwise the specimen would receive an undesired compressive stress wave.

A number of research works have designed the interruption of SHTB experiments. In the beginning of 90s, a method to interrupt Hopkinson experiments was developed by Nemat-Nasser *et al* [25], which was based on the absorption of the reflected waves for controlling the deformation level of the specimen. Ma *et al* [26] developed a high-speed tensile facility to interrupt the fracture tests for pure copper specimen at different levels of elongation. El-Saeid Essa *et al* [27] developed a convenient approach to interrupt a SHTB test, which is described below. They modified the ends of the incident and transmission bars, and used an external interruption fixture to control the deformation level of the specimen. Such system can control the elongation of specimens at high strain rate using a modified SHTB.

The influence of the designed external fixture on the stress waves and also the ability of the system to support the interruption of the deformation process must be considered in the numerical analysis and verified by the experimental results. Strain–stress responses at various strain rates is an important aspect of the dynamic behaviour of materials up to the point where

the specimen breaks. A modified SHTB on which an external interruption fixture was mounted was developed by González-Lezcano *et al* and installed in the Universidad Carlos III de Madrid Engineering Laboratory (Madrid, Spain), as detailed in [28]. The external interruption fixture stops the test at predetermined elongation before reaching the material's failure strength. The system developed in 2003 included damping rings to attenuate the effects of the compressive waves produced as result of including the external interruption fixture. Different materials were considered for the damping rings, such as lead and polypropylene.

In the modified SHTB apparatus, the bars are designed with a non-uniform cross section. Moreover, an increment of the cross-sectional area of the bar ends which are in contact with the specimen is necessary to properly mount the external interruption fixture in parallel with the bars, as shown in figure 8. Such increment of the cross-sectional area of the above-mentioned bar ends does not significantly interfere on the classical SHTB apparatus behaviour, as discussed below.
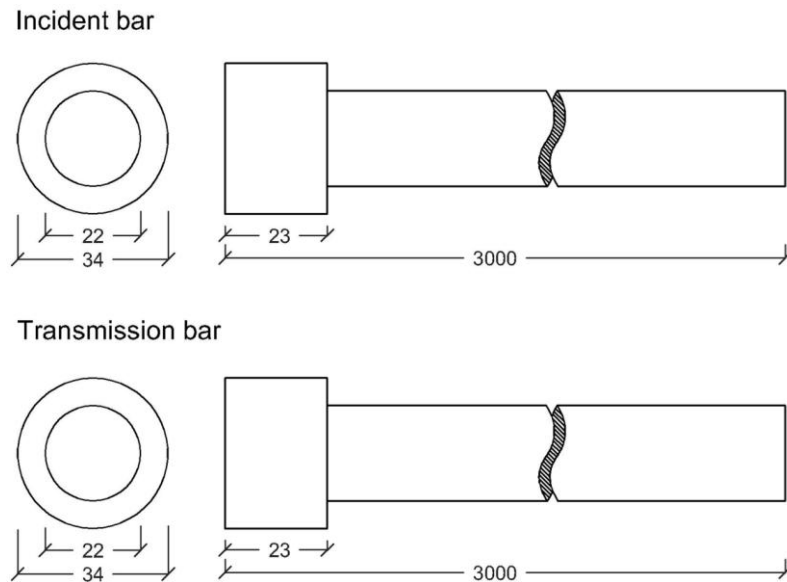
Figure 8. Front view and side view of the incident and transmission bars with an increment of the cross-sectional areas of their ends.

Figure 9 shows the front view of the above-mentioned modified SHTB installed in the Universidad Carlos III de Madrid Engineering Laboratory (Madrid, Spain), including (A) the external interruption fixture (i.e., a cylindrical element that consists of two steel pieces that are screwed to facilitate a proper access to the specimen), (B) an increase of the cross-sectional area of the bar ends to which the specimen is screwed (as shown in fig. 8), and (C) two damping rings made of a buffer material placed on the interface between the bars and the external interruption fixture.
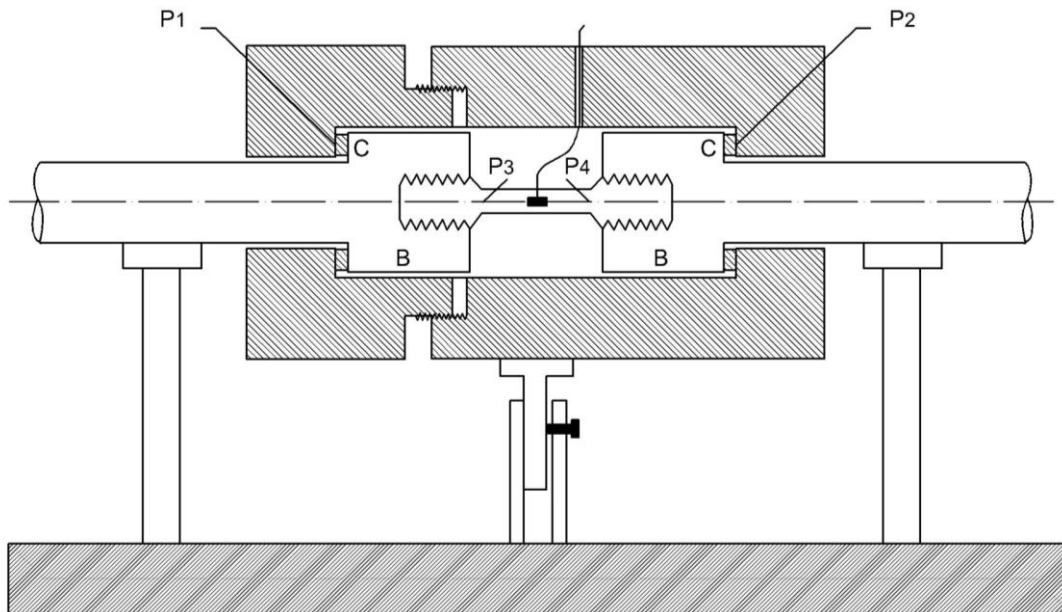
Figure 9. Front view of the external interruption fixture mounted on a modified SHTB. (A): external interruption fixture mounted in parallel with the bars. (B): increase of the cross-sectional area of the bar ends to which the specimen is screwed, and (C): damping rings.

Following the ASTM Standards and Recommendations [29] and Rodríguez [30], tension specimens are generally dog-bone shaped. They are placed in specially designed grips screwed into the threaded incident and transmission bars. Tension specimens with threaded ends are generally fabricated from 6.35-mm diameter bar stock. To accept the threaded specimen, aluminum anvils are attached to the incident and transmission bar ends with threaded holes. The length of reduced section of the specimen (L) is 25.4 mm long, the diameter of such reduced section (D) is 6.35 mm long, the threaded zone diameter (D_r) is 12 mm long, and the threaded zone length (L_r) is 14 mm long.

Figure 10. Specimen

The interruption fixture performs as an actual rigid body avoiding the expansion of the damping rings. Therefore, the damping rings deform when the specimen deforms. This can be achieved fabricating a robust element with the suitable mechanical properties and whose dimensions are consistent with the aim pursued. The interruption fixture maintains a constant length between

the damping rings allowing them to stop the experiment. The elongation of the test specimen can therefore be controlled by the length of the external interruption fixture. The element is manufactured in two threaded pieces to permit an easy access to the specimen. The damping rings can be suitaby adjusted by means of the threaded pieces. Figure 11 shows a picture of the two-piece external interruption fixture when (a) unscrewed to insert the damping rings or access the specimen and when (b) screwed.
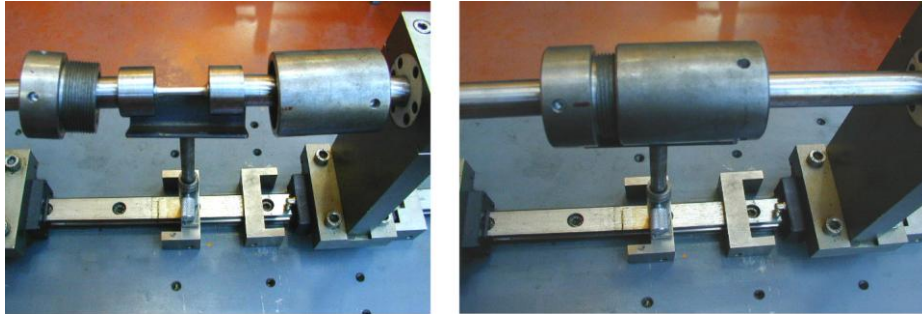
Figure 11. External interruption fixture when (a) unscrewed to insert the damping rings or access the specimen and (b) when screwed.

The interruption fixture is mounted on a support to avoid friction with the bar ends. Figure 12 shows the dimensions of the interruption fixture used in the FE model.
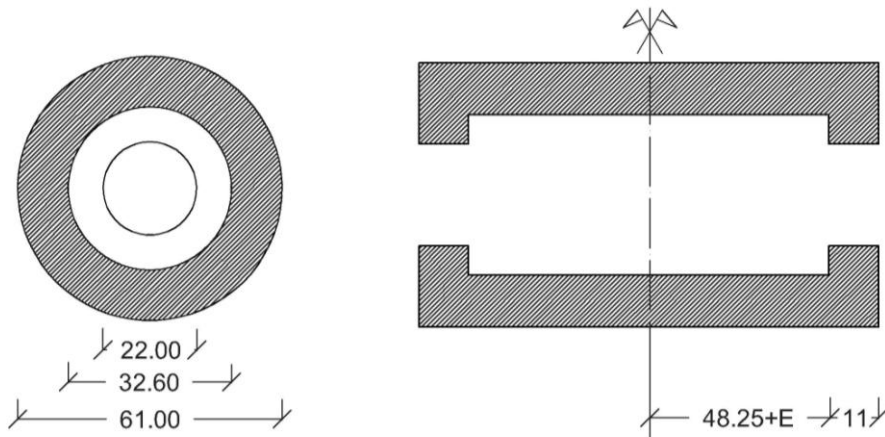
Figure 12. Front and side views of the interruption fixture used in the FE model (dimensions in mm).

Figure 13. 30-mm inner diameter and 3-mm thick damping disks

The damping rings shown in figure 13 are enclosed in the interruption fixture and they are responsible for allowing the specimen deformation. Their main purpose is allowing deformation in the specimen until the maximum strain before failure strength can be reached. In addition, it

can be observed that the damping rings enter a wide zone of plastic deformation. Such plastic deformation actually absorbs the undesired compressive stress wave. Homogeneous stress and strain in the specimen are considered. However, the stress distribution depends on the stress pulse applied.

Damping rings must be designed to adjust the material being tested. The election of the material is extremely important since they must be ductile enough for energy absorption and strong enough to attenuate the incident wave.

When using the external interruption fixture, the stress-strain curve cannot be obtained. However, the strain gauge placed at the maximum strain zone yields a proper strain-time curve. Therefore plastic wave theory should be applied. The resultant differential force obtained when setting up the equilibrium condition of the tension forces acting on a differential element of the bar [31] is given by

$$A \cdot \delta\sigma/\delta x \cdot dx = \rho \cdot A \cdot dx \cdot \delta^2 u/\delta t^2 \qquad (36)$$

In this case, the relation between stresses and strains is a non-linear relation and therefore Hooke's law does not apply. On the contraty, the variation of the stress-strain curve slope should be considered when entering the plastic zone.

$$\text{slope} = \delta\sigma/\delta\varepsilon, \text{ which is a function of the strain } (\varepsilon) \qquad (37)$$

The equation may therefore be expressed as follows:

$$\delta^2 u/\delta t^2 = (\delta\sigma/\delta\varepsilon) / \rho \cdot \delta^2 u/\delta x^2 \qquad (38)$$

or, when considering that the speed of the stress wave is a function of the strain, it could be rearranged as:

$$\delta^2 u/\delta t^2 = c^2 (\varepsilon) \cdot \delta^2 u/\delta x^2 \qquad (39)$$

The relation between stress and velocity is simple in an elastic wave since the speed of the stress wave is constant. In the elastic-plastic case, a deeper study must be accomplished, as discussed below. When the stress wave produces an elastic-plastic deformation on the element, then

$$dt = dx / (\sqrt{(d\sigma / d\varepsilon)_1 / \rho}) \qquad (40)$$

where ρ is density and σ_1 and ε_1 are the plastic stress and the plastic strain respectively. Considering the momentum conservation equation,

$$(\rho A \, dx) \, dv = A \, d\sigma_1 \, dt \qquad (41)$$

Hence,

$$dv = d\sigma / (\rho \cdot (\sqrt{((d\sigma / d\varepsilon)_1 / \rho)})) \qquad (42)$$

where dv is the differential velocity of the element when the stress wave propagates within.

$$d\sigma = (d\sigma / d\varepsilon)_1 \, d\varepsilon \tag{43}$$

$$dv = (\sqrt{(d\sigma / d\varepsilon)_1 / \rho}) \, d\varepsilon \tag{44}$$

The desired relation can be obtained by integration.

$$v = \int_0^{\varepsilon_1} \sqrt{\frac{(d\sigma/d\varepsilon)_1}{\rho}} d\varepsilon = \int_0^{\varepsilon_1} c(\varepsilon_1) d\varepsilon \tag{45}$$

and the relation between stress and velocity can therefore be found.

$$\sigma = \rho \, c(\varepsilon_1) \, v \tag{46}$$

The speed of the stress wave [$c(\varepsilon_1)$] can be obtained from the stress-strain curve [32].

5. Finite element (FE) simulations methodology.

The finite element (FE) method method is a powerful technique originally developed for numerical solution of complex problems in structural mechanics and it remains the method of choice for complex systems. In this paper the FE simulations are performed using the finite element program ABAQUS (from ABAQUS, Inc.). The finite element models described herein are created with ABAQUS/CAE [33]. ABAQUS/Explicit code is used for the calculations to study the precise dynamical phenomena in the specimen. Instances are meshed using quadrilateral elements (CAX4R) and a structured meshing. In general, structured meshing provides the most control over the mesh that ABAQUS/CAE generates. ABAQUS/CAE respects seed distribution wherever possible when generating a structured mesh.

For modelling, a strain-rate sensitive model is employed. The model is complemented by assuming that the transverse stresses are zero. A 1D code is developed on the basis of the Godunov scheme [34].

Three FE models are established. A classical SHTB model without the external interruption fixture (Model-1), a modified SHTB model increasing the cross-sectional area of the bar ends which are in contact with the specimen but without the external interruption fixture (Model-2), and a modified SHTB model with the entire interruption device including the fixture and the damping rings enclosed within (Model-3). Figures 14, 15, and 16 show details of the three FE simulated models.

Figure 14. Classical SHTB without interruption (Model-1).

Figure 15. Modified SHTB when the cross-sectional area of the bar ends which are in contact with the specimen is increased but without assembling an external interruption device (Model-2).
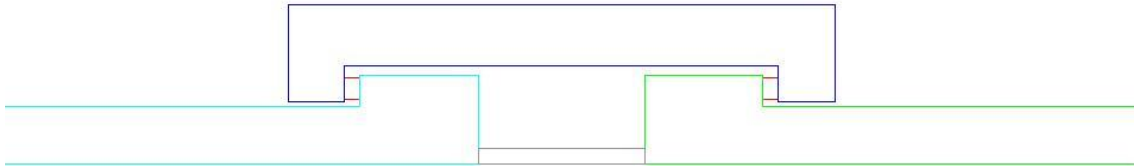
Figure 16. Modified SHTB when using damping rings enclosed in an external interruption fixture. (Model-3).

Finite element simulations of high-strain-rate tension experiments have been performed on Aluminum 7017-T73 alloy specimens using different dimensions of the damping rings made of lead at a strain rate of 1,000 s^{-1} in order to reproduce the same stress wave observed in experiments accomplished with SHTB apparatus. The classical SHTB (Model-1) has already been validated with the SHTB apparatus in which high strain rate tensile experiments are made on Aluminum 7017-T73 alloy specimens [35]. The modeling results of Model-1 correlate well with the SHTB experimental results when carried out without interruption, confirming the validity of the FE model.

The strike is modeled by a rigid body impacting the end of the incident bar. The incident and transmitted waves are achieved in the same nodes of the FE model, which correspond to the strain gauge positions on the real bars.

Details of FE meshes of the three models for validating interrupted mechanisms can be found below: the classical SHTB model without interruption (Model-1 shown in fig. 17), the modified SHTB model when the cross-sectional area of the bar ends which are in contact with the specimen are increased but without assembling the interruption device (Model-2 shown in fig. 18), and the modified SHTB model with the entire interruption mechanism (Model-3 shown in fig. 19).

Figure 17. Structured mesh in the classical SHTB model without interruption (Model-1).

Figure 18. Structured mesh in the modified SHTB model when the cross-sectional area of the bar ends which are in contact with the specimen is increased (Model-2).
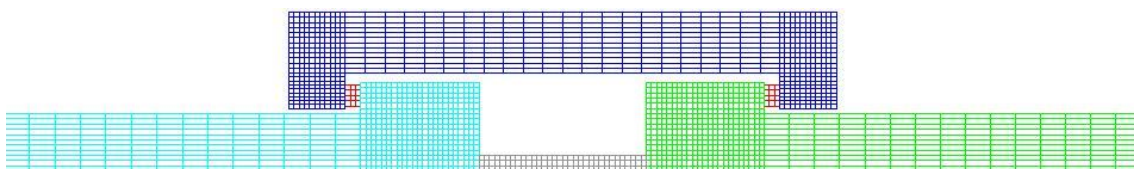
Figure 19. Structured mesh in the modified SHTB model with the entire interruption mechanism including the damping rings (red zones) enclosed in the interruption fixture (blue zones). (Model-3).

The numerical models of both the classical SHTB model (Model-1) and the modified SHTB model when the cross-sectional area of the bar ends which are in contact with the specimen is increased (Model-2) consist of:

- Number of nodes: 10,596
- Number of elements: 9,678

The numerical model of the modified SHTB model when using an interruption device including two damping rings enclosed in an interruption fixture (Model-3) consists of:

- Number of nodes: 11,437
- Number of elements: 10,428

6. Results

Numerical simulations on both classical SHTB model (Model-1) and modified SHTB model when the cross-sectional area of the bar ends which are in contact with the specimen is increased (Model-2) are accomplished at a strain rate of 1,000 s^{-1} for comparison purposes. The differences between them are minimal. Thereafter, numerical simulations on both modified SHTB model when the cross-sectional area of the bar ends which are in contact with the specimen is increased (Model-2) and modified SHTB model when using damping rings enclosed in an interruption fixture (Model-3) are accomplished for comparison purposes.

The incident waves from the three FE models are almost identical, since they are measured before the interruption device is assembled. Figures 20 and 21 compare the results of Model-1 and Model-3 at the strain rate of 1,000 s^{-1}.

The transmitted waves obtained in Model-1 and Model-2 are similar, which reflects the fact that the increase of the cross-section of the bars does not affect the quality of the transmitted wave. The reflected wave of Model-3 is different from that of Model-1 and Model-2, suggesting that the interruption device can absorb part of the reflected wave.
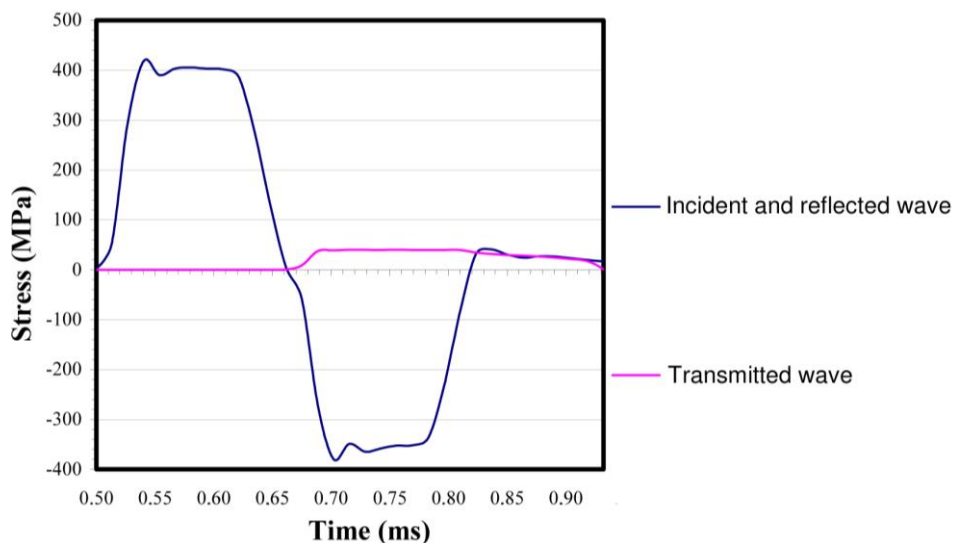
Figure 20. Stress waves in classical SHTB model (Model-1).
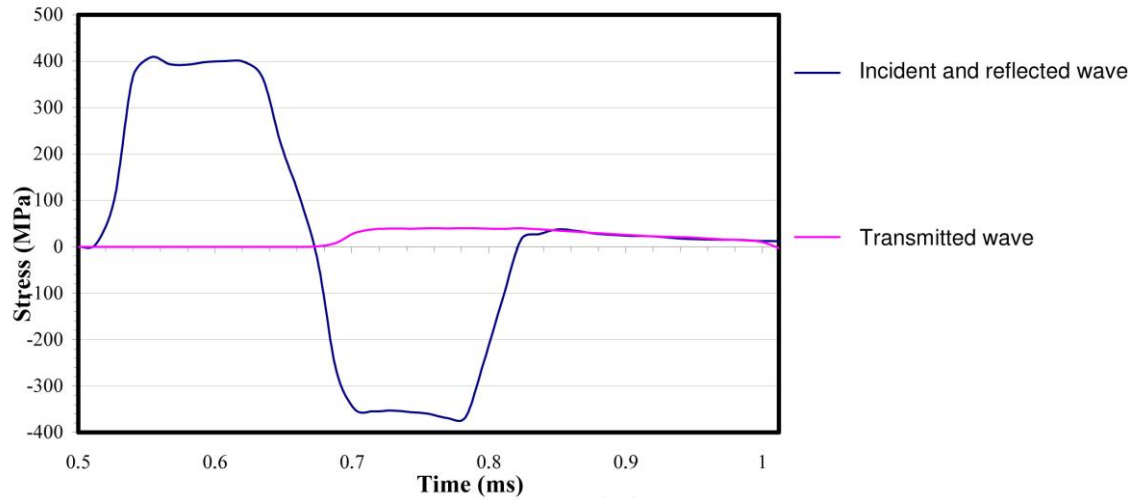
Figure 21. Stress waves in the modified SHTB model (Model-2).

The comparison of incident and reflected waves for Model-1 and Model-2 are shown below.
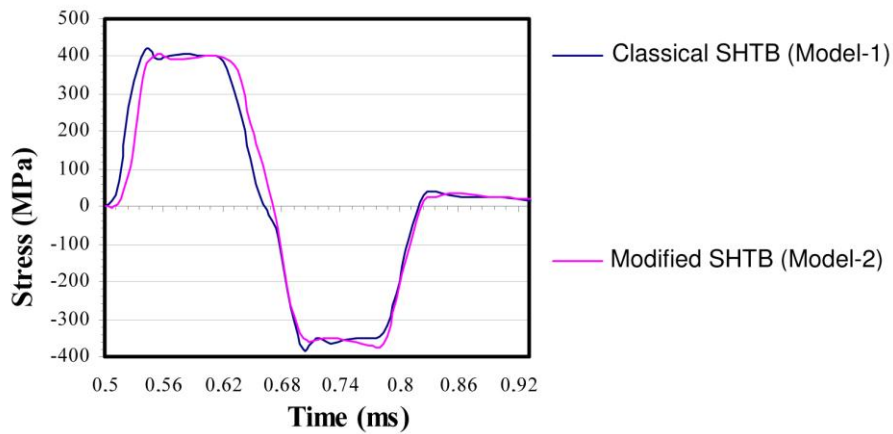
Figure 22. Incident and reflected stress waves observed in Model-1 and Model-2.

Though the Model-1 node in which stress wave is taken slightly differs from the Model-2 node, the peaks observed in each case are similar except for the initial peak, which happens to be higher in Model-1.
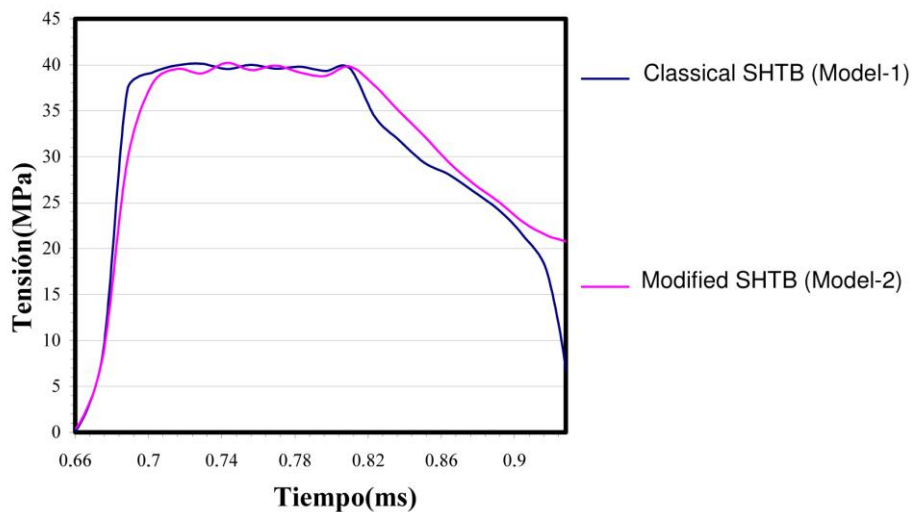
Figure 23. Transmitted stress waves through the transmission bar in Model-1 and Model-2.

It can be observed that both curves match approximately, although the modified SHTB (Model-2) stress wave is slightly delayed.
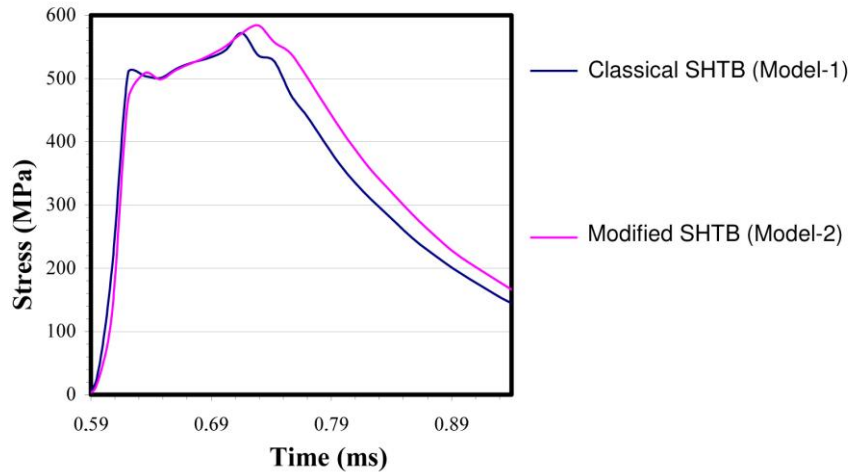
Figure 24. Stress waves in the centre of the specimen in Model-1 and Model-2.

Stress waves transmitted in modified SHTB models both without interruption (Model-2) and with the external interruption device (Model-3) are shown below.

When mounting the interruption device to modify the classical SHTB, the 1D stress wave propagation assumption becomes a challenging issue since the stress waves present deviations. The stress waves transmitted in both modified classical SHTB without interruption (Model-2) and modified SHTB including the interruption device (Model-3) are discussed below.
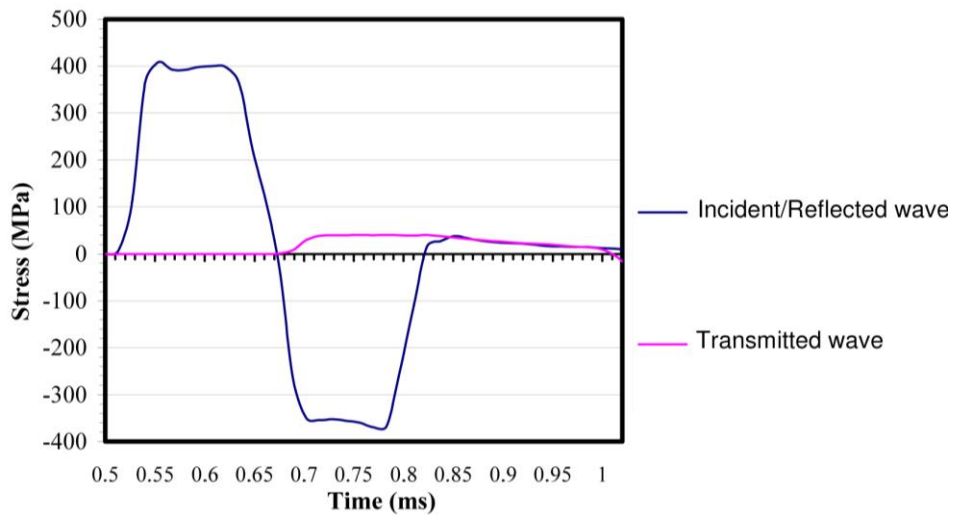
Figure 25. Stress waves in the modified SHTB without interruption (Model-2).
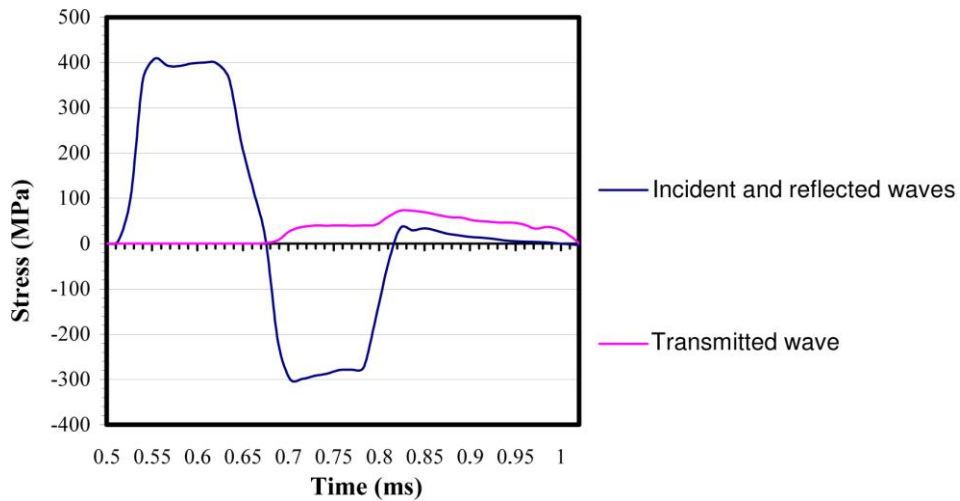
Figure 26. Stress waves in the modified SHTB using 4-mm thick damping rings made of lead (Model-3).

The comparison of incident and reflected waves for Model-2 and Model-3 are shown below.
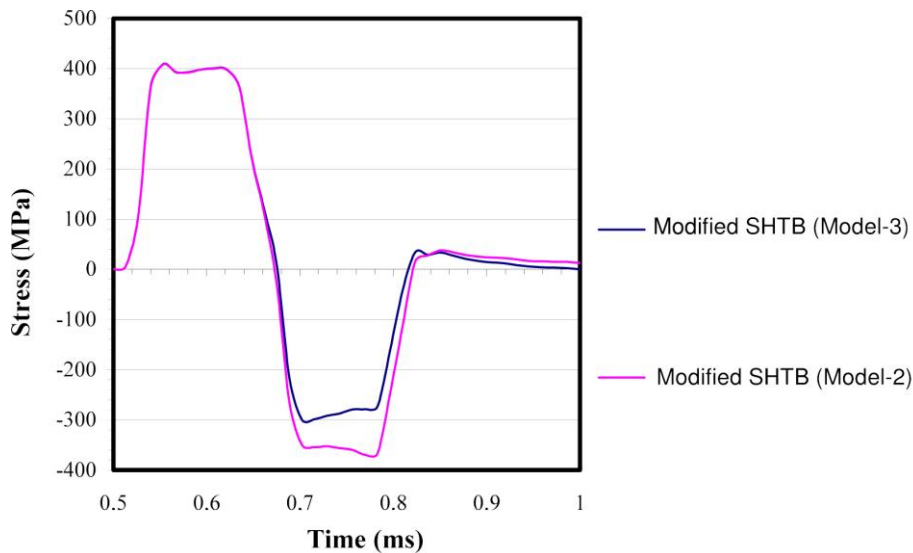
Figure 27. Incident and reflected stress waves in both modified SHTB without interruption (Model-2) and modified SHTB including the interruption device (Model-3).

Figure 27 shows that incident waves overlap. However, the reflected waves present significant discrepancies due to the presence of the interruption device, which partly absorbs the incident wave before it reaches the bar end. The stress-time curves show that the reflected wave is considerably different in each case. Actually, the wave transmitted to the specimen in Model-3 is lower than that of the Model-2.

Ultimately, the difference between both models lies on the fact that in the modified SHTB with the interruption device (Model-3) the transmitted wave travels through two different paths (i.e., the specimen and the interruption device), while in the modified SHTB without interruption (Model-2) the transmitted wave only travels through the specimen.

Therefore, transmitted waves to the specimen should be compared in order to investigate whether the pulse in the specimen reduces in Model-3 with respect to Model-2. Stress values in the centre of the specimen are represented below.
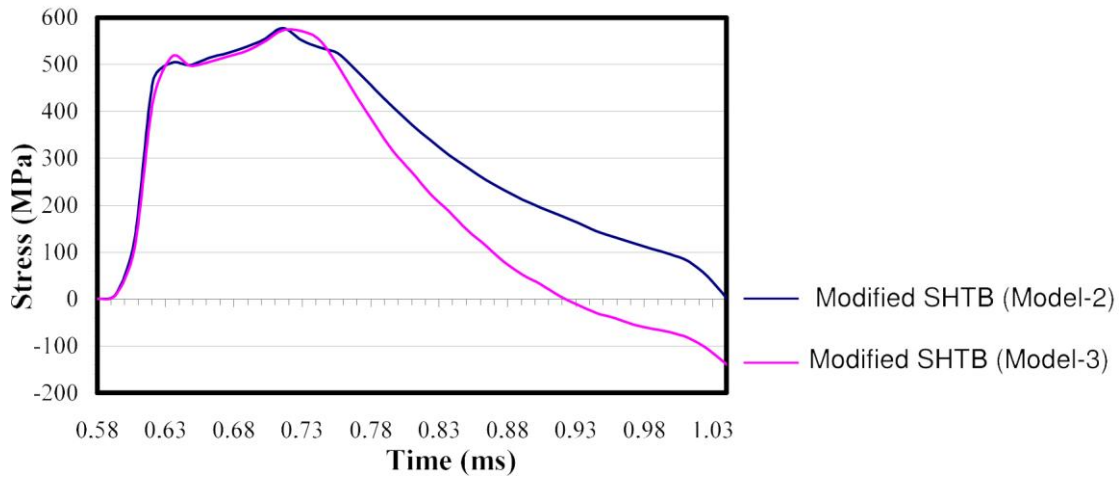
Figure 28. Stress waves in the centre of the specimen for both modified SHTB without interruption (Model-2) and modified SHTB including the interruption device (Model-3).

Figure 28 shows that the stress peak in the specimen is higher in Model-2, as expected. Therefore, it can be deduced that part of the transmitted wave is traveling through the interruption device. The tensile stress wave in the specimen is attenuated in Model-3 in comparison with Model-2. The peak varies from values exceeding ultimate tensile strength of the specimen in Model-2 to values under its ultimate tensile strength in Model-3. This issue is discussed below.

The stress reduction as time increases is due to the compressive wave transmitted by the interruption device into the increased cross-sectional area of the incident bar and, thereafter, to the specimen. Since the stress distribution in the specimen must be tensile in a SHTB experiment, such stress reduction could enhance the compressive wave and therefore the specimen could buckle due to its slenderness ratio.

In order to observe the wave absorbed by the interruption device, the stress produced in the interface between the damping rings and the incident bar is measured in the node spotted in figure 29.
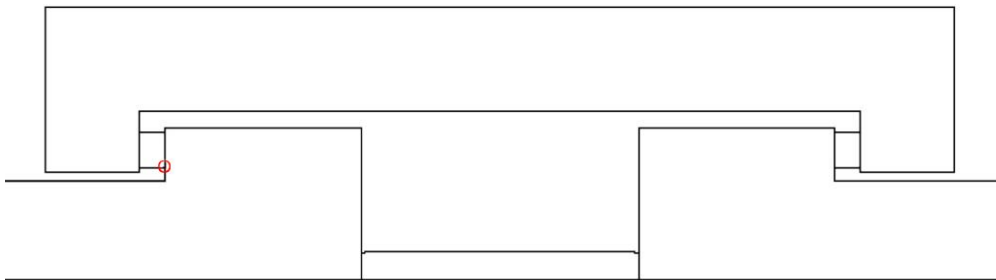
Figure 29. Node analysed in fig. 30

- 19 -
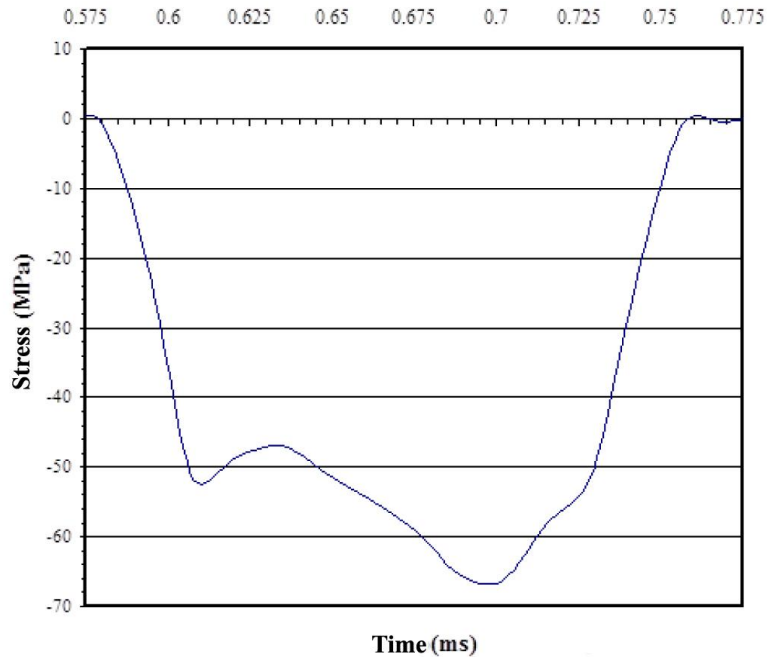
Figure 30. Stress in the node placed on the interface between the incident bar and the damping rings.

Inasmuch as the yield strength of lead is 33 MPa and the stress values in the damping rings are up to 65 MPa, it can be observed that the damping rings enter a wide zone of plastic deformation. Such plastic deformation actually absorbs the undesired compressive stress wave. The performance accomplished by the interruption device can be in-depth studied by analysing the stress waves in the transmission bar, as shown below.
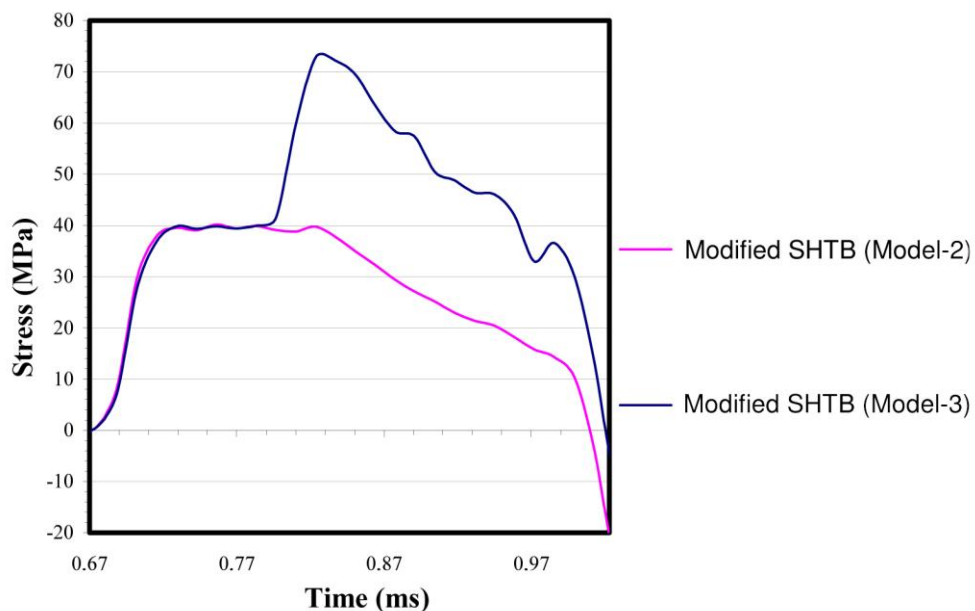
Figure 31. Stress waves through the transmission bar in both modified SHTB without interruption (Model-2) and modified SHTB with the interruption device (Model-3).

The transmitted waves relative to both Model-2 and Model-3 overlap during the range between 0.67 and 0.77 ms. However, a peak is observed when time exceeds 0.77 ms in Model-3 as shown in figure 30. This peak appears when the interruption device is put into operation.

Figure 32 below shows the node placed on the interface between the transmission bar and the damping rings in which stresses are analysed.
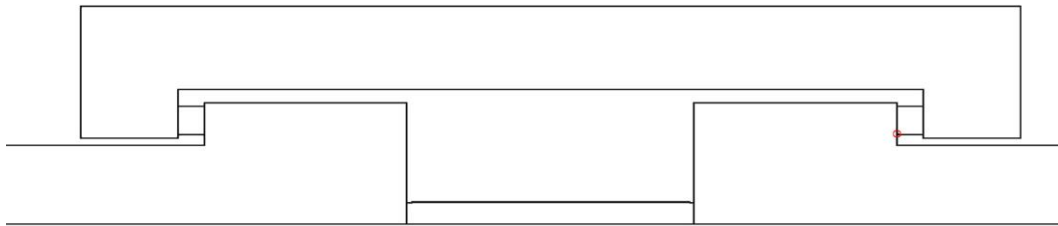
Figure 32. Node analysed in figure 32
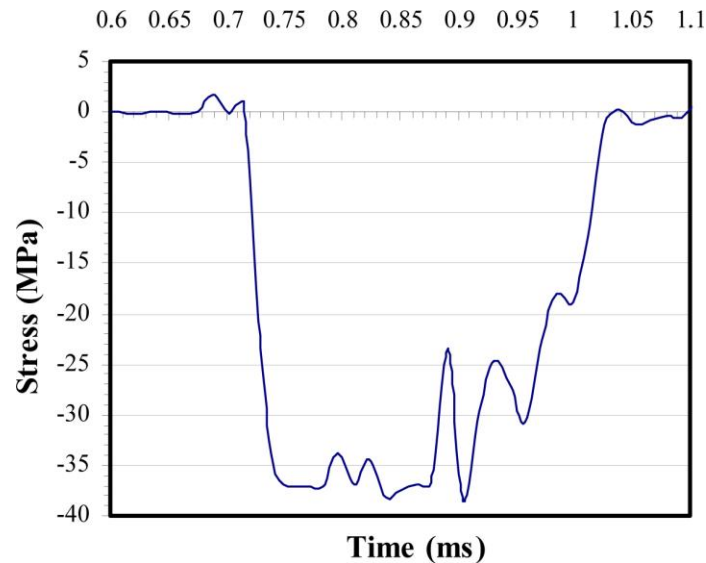
Figure 33. Stress wave in the interface between the damping rings and the transmission bar.

Figure 33 shows the wave actually transmitted between the damping rings and the transmission bar. Its peaks have the same order of magnitude than the yield strength of lead. This wave is delayed with respect to the wave passing through the specimen due to the difficulties found while getting through the damping rings. It can be demonstrated identifying the instants t_1 = 7.16E-1 ms and t_2 = 7.97E-1 ms when the stress wave is about to reach the interface between the damping rings and the transmission bar at a distance of 40 cm from the transmission bar end. Such distance can be computed using Eq. 47.

$$d = \Delta T \cdot c \tag{47}$$

where d is the distance between two points, c is the speed of a wave through steel (c = 5072.72 m/s) and $\Delta T = t_2 - t_1$ = 7.97E-4 – 7.16E-4 = 8.1E-5 s. Therefore, d = 0.41 m = 41 cm.

It can be demonstrated that the interruption device is responsible for the wave transmission according to the gap shown in fig. 30 between the modified SHTB without interruption (Model-2) and the modified SHTB including the interruption device (Model-3).

Ultimately, the robustness of the interruption device is studied. The system limits the specimen deformation by means of the damping rings enclosed within. The interruption fixture must be robust enough to bear the effect of the compressive wave and allow the damping rings to work properly.

As expected, the interruption fixture performs as a rigid body according to the negligible relative displacement of its ends.

Similar behaviours are observed between Model-2 and Model-3, but significant discrepancies can also be found. 1D stress wave propagation theory does not apply to study stress-strain curves in the specimen. In Model-3 it is necessary to mount one (or even more than one) strain gauge on the specimen, always provided that stress values do not reach failure strength. Consequently, strains in the specimen as a function of time can be directly obtained from the specimen instead of being computed from the division of the transmitted wave which is partly transmitted to the specimen and partly transmitted to the interruption device.

The plastic behaviour of the specimen must be considered when strains in the specimen are studied directly. Therefore, obtaining stress-strain curves for a given strain rate becomes necessary. However, it is more suitable to collect the data directly from the experimental tests. The stress-strain curve can be experimentally found by means of the classical SHTB, in which plastic deformation zones before failure strength can be properly studied.

Figures below show the instants when higher stresses and strains are found in the specimen. Figure 34 shows the incident wave approaching to the interruption device at instant t_1 = 5.4 E -1 ms.
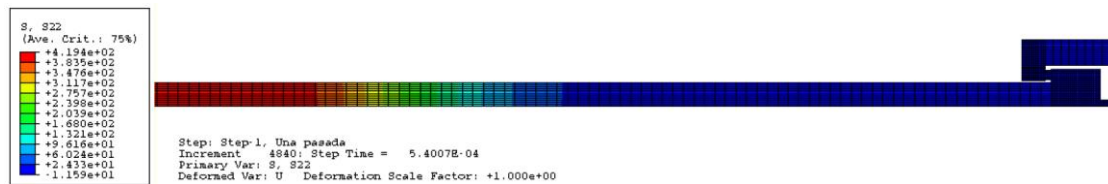
Figure 34. Incident wave approaching to the interruption device at instant t_1 = 5.4 E-1 ms (general view).
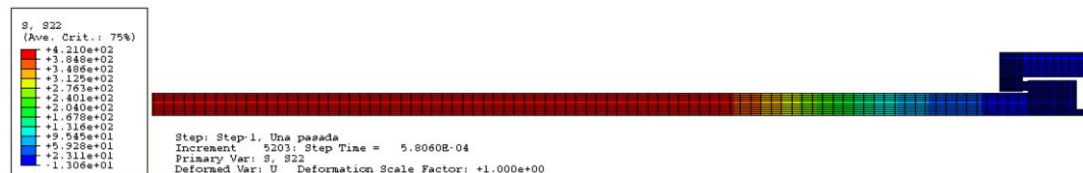
Figure 35. Incident wave approaching to the interruption device at instant t_2 = 5.806 E-1 ms (general view).

Figure 36 shows the incident wave entering the interruption device at instant t_3 = 5.941 E-1 ms.
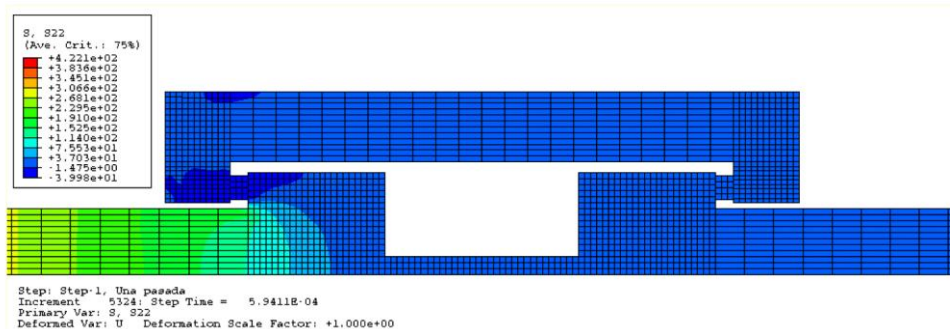
Figure 36. Incident wave approaching to the interruption device at instant t_3 = 5.941 E-1 ms (enlargement of the interruption device).
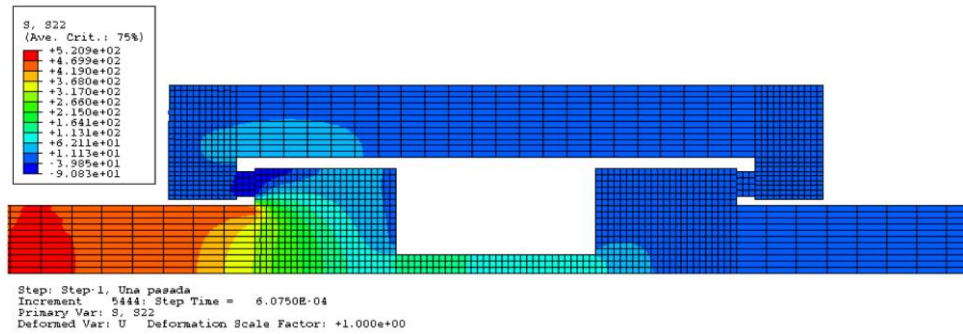
Figure 37. Incident wave approaching to the specimen at instant t_4 = 6.075 E-1 ms (enlargement of the interruption device).

Figure 37 shows that the wave enters at a higher rate through the centre (i.e., through the specimen) and it results stopped when reaching the left damping ring.
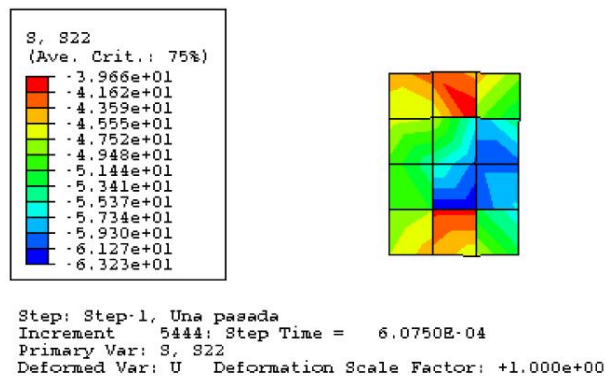

Figure 38. Incident wave in the left damping ring at instant t_4 = 6.075E-1 ms (enlargement of the left damping ring).

At instant t_4 = 6.075E-1 ms the left damping ring shows a plastic regime in yellow, orange, and red zones. The entire damping rings must deform plastically to perform an effective opposition to the compressive wave. At t_5 = 6.345 E-1 ms the specimen enters a high-stress zone.
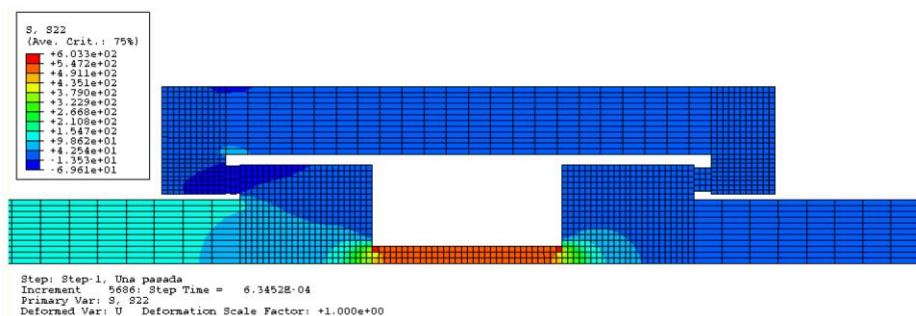
Figure 39. Specimen entering a high-stress zone at instant t_5 = 6.345 E-1 ms (enlargement of the interruption device).

Figure 39 shows that the stress values at the specimen exceeds its yield strength (507 MPa) in both the green area and the red corners.
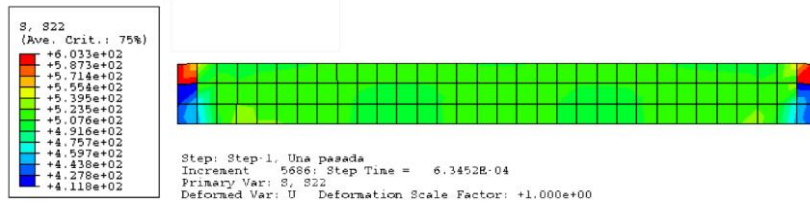
Figure 40. Specimen entering a high-stress zone at instant $t_5 = 6.345$ E-1 ms. (enlargement of the specimen).

In the actual experiment this stress concentration at the corners is avoided by means of the radius of curvature of the corners. Therefore, the numerical study is focused in the central area of the specimen, where maximum stress distribution is observed.
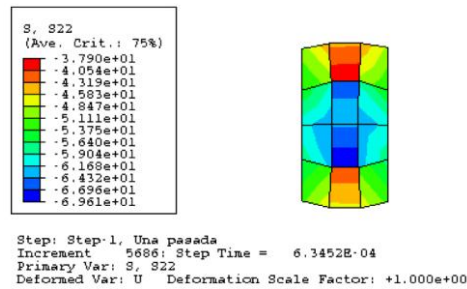

Figure 41. Left damping ring entering high-stress zones at instant $t_5 = 6.345$E-1 ms (enlargement of the left damping ring).

Figure 41 shows a similar situation than that of figure 38, in which the left damping ring is showing a plastic stress distribution. The stress in the specimen increases in the forthcoming instants while the interruption device is working optimally.
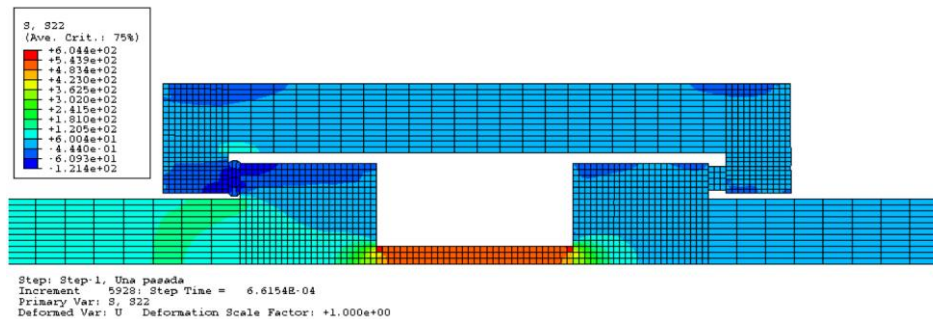
Figure 42. Plastic deformation of the specimen and the left damping ring at instant $t_6 = 6.615$ E-1 ms (enlargement of the interruption device).

In figures 43 and 44 the specimen and the left damping ring are shown separately to clearly show the magnitude of their stress distribution.
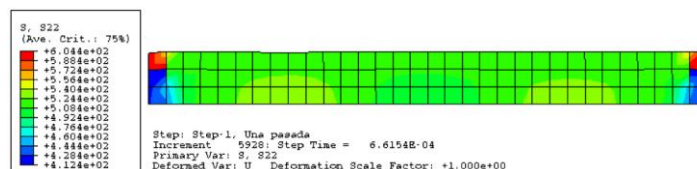

Figure 43. Specimen entering a plastic deformation zone at instant $t_6 = 6.615$ E-1 ms (enlargement of the specimen).

Figure 44 shows the left damping ring suffering plastic deformation at instant $t_6 = 6.615$ E-1 ms and significantly opposing the incident pulse.
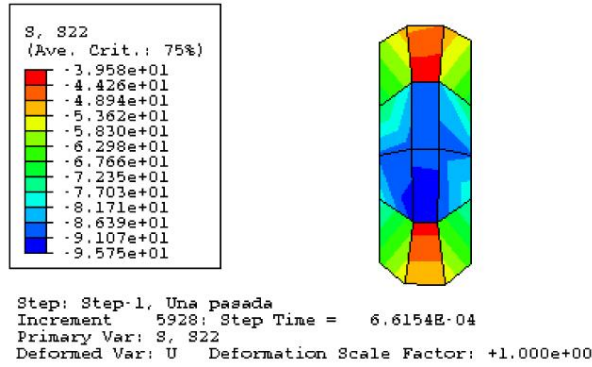
Figure 44. Left damping ring entering a plastic deformation zone at instant $t_6 = 6.615$ E-1 ms (enlargement of the left damping ring).
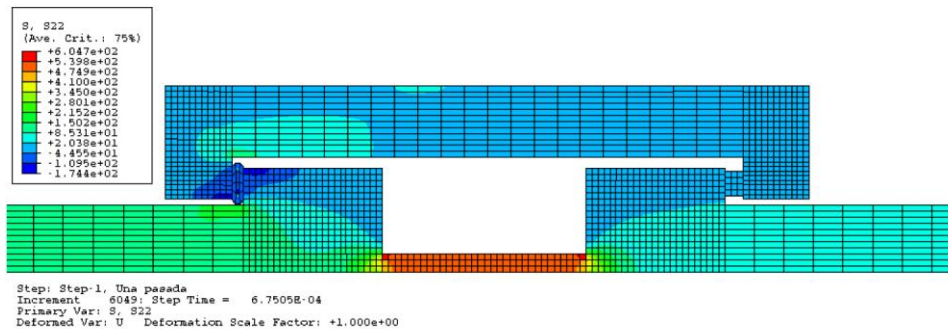

Figure 45. Stress wave entering the transmission bar at instant $t_7 = 6.75$ E-1 ms (enlargement of the interruption device).

Figure 45 illustrates the instant $t_7 = 6.75$ E-1 ms, in which the transmission bar is under a tensile stress distribution derived directly from the specimen. In addition, the right damping ring is transmitting a stress wave due to the optimal interruption of the process. The interruption fixture and the damping rings are depicted below for an in-depth study of this process.
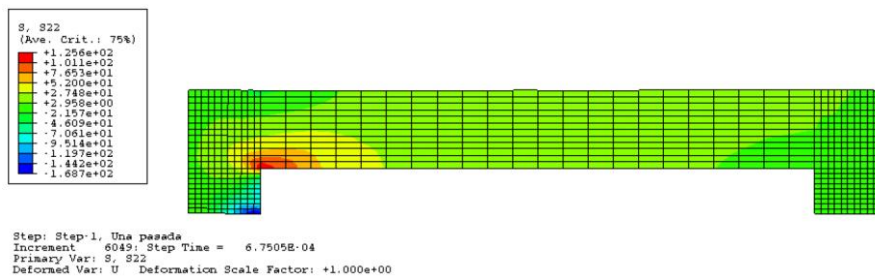
Figure 46. Stress wave distribution in the interruption fixture at instant $t_7 = 6.75$ E-1 ms (enlargement of the interruption fixture).

Figure 46 illustrates that a tension pulse initiates as a consequence of the high compressive state generated in the interface between the incident bar and the left damping ring. Thereafter, it can be observed that stress values in the interface between the right damping ring and the transmission bar is a low-stress zone at instant $t_7 = 6.75$ E-1 ms. The pulse transmitted to the transmission bar derives solely from the specimen, as previously discussed.

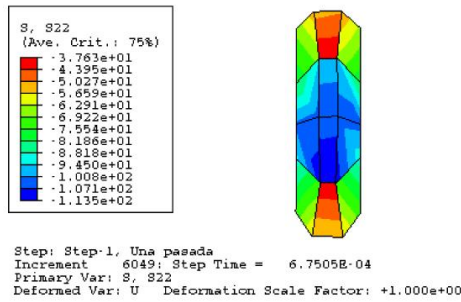Figure 47 shows the left damping ring deforming plastically at instant $t_6 = 6.75$ E-1 ms.

Figure 47. Plastic deformation of the left damping ring at instant
$t_6 = 6.75$ E-1 ms (enlargement of the left damping ring).

The wave transmitted by the interruption device reaches the transmission bar at instant $t_8 = 7.02$ E-1 ms, as shown in figure 48.
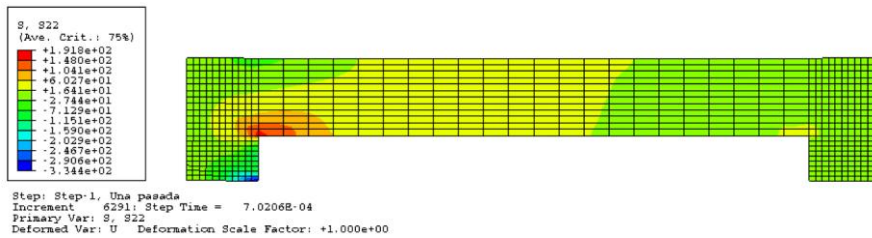

Figure 48. Stress wave distribution in the interruption fixture at instant $t_8 = 7.02$ E-1 ms
(enlargement of the interruption fixture).

Figure 49 illustrates the right damping ring entering a compressive zone while transmitting the stress wave to the transmission bar.
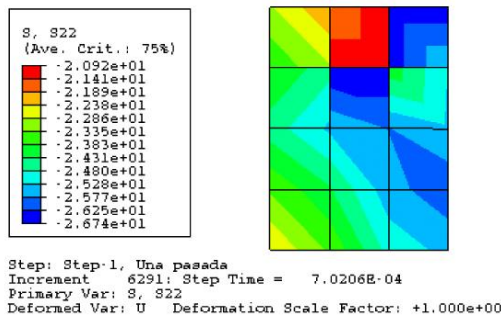

Figure 49. Stress distribution in the right damping ring at instant

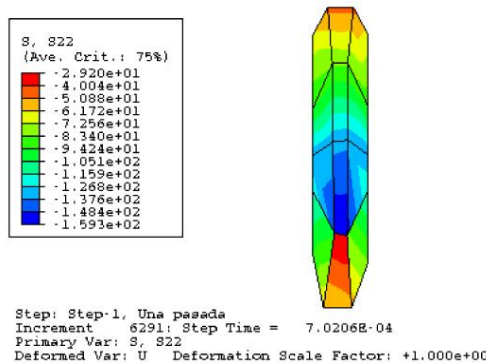*$t_8 = 7.02$ E-1 ms (enlargement of the right damping ring).*

Figure 50. Stress distribution in the left damping ring at instant
$t_8 = 7.02$ E-1 ms (enlargement of the left damping ring).

Figure 50 shows the left damping ring suffering its maximum stress value at instant t_8=7.02 E-1 ms. It can be observed that lead is performing values beyond its failure strength. Moreover, the specimen reaches the maximum stress values at instant t_9 = 7.29 E-1 ms (figure 51). After such instant the stress in the specimen decreases until compressive values are reached.
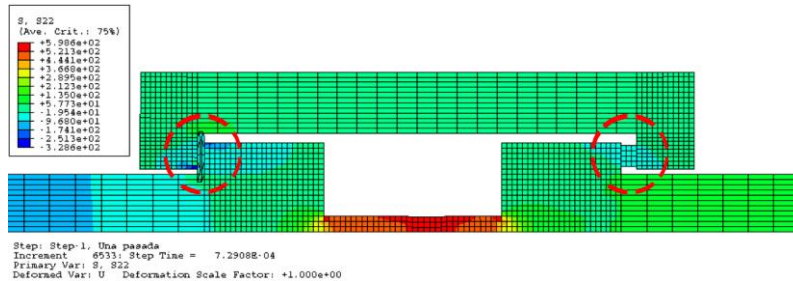

Figure 51. Maximum stress values in the specimen at instant t_9 = 7.29 E-1 ms (enlargement of the interruption device).

Figure 51 shows the instant of maximum stress values in the specimen (see red area at the centre of the specimen). It can also be observed the different mechanical behaviours in both left and right damping rings. An enlarged representation of the specimen is shown in figure 52.
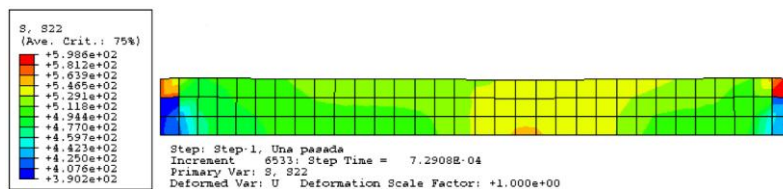

Figure 52. Maximum stress values in the specimen at instant t_9 = 7.29 E-1 ms (enlargement of the specimen).

The stress reaches a maximum value of 570 MPa at the centre of the specimen (see yellow and orange areas) at t_9 = 7.29 E-1 ms. Figure 53 shows the wave transmission in the interruption fixture at the same instant.

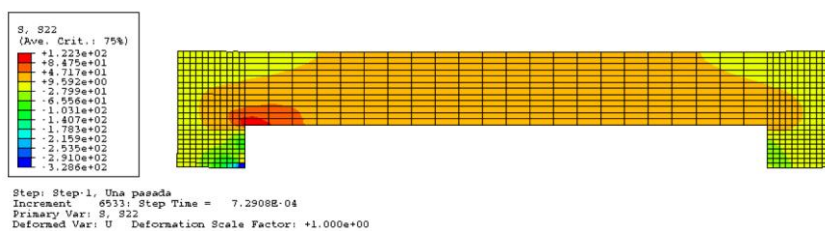*Figure 53. Stress distribution throughout the interruption fixture at instant t_9 = 7.29 E-1 ms (enlargement of the interruption fixture).*

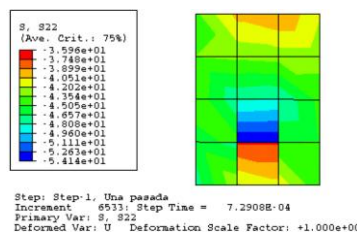*Figure 54. Stress distribution in the right damping ring at instant t_9 = 7.29 E-1 ms (enlargement of the right damping ring).*

Figure 54 shows an enlargement of the right damping ring while transmitting the maximum stress value. Figure 55 shows the evolution of the stress wave through the interruption device and the specimen at instant t_{10} = 7.696 E-1 ms, in which a reduction of the stress values in the specimen can be observed whilst the transmission bar is suffering the maximum stress values. It can be observed that the stress values in the right damping ring are compressive.
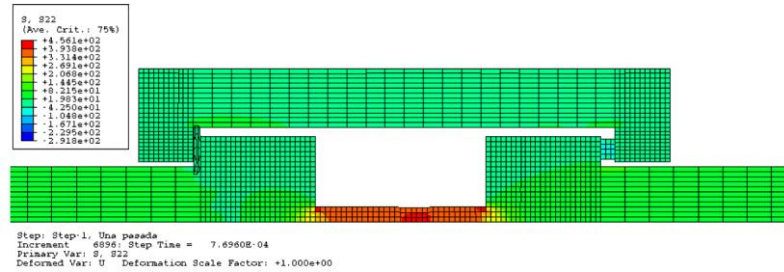

Figure 55. Reduction of stress values in the specimen at instant t_{10} = 7.696 E-1 ms.

Figure 56 shows an enlargement of the right damping ring in which only a compressive stress distribution can be observed.
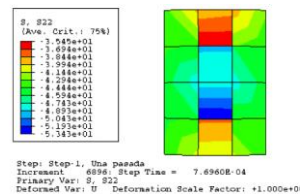

Figure 56. Stress distribution in the right damping ring at instant
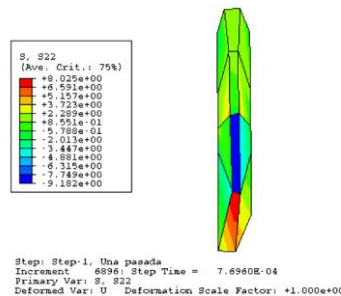*t_{10} = 7.696 E-1 ms (enlargement of the right damping ring).*

Figure 57. Stress distribution in the left damping ring at instant
t_{10} = 7.696 E-1 ms (enlargement of the left damping ring).

Figure 57 shows an enlargement of the left damping ring in which the areas of low tensile stress values coexist with the areas of low compressive stress. It can be deduced that the damping ring finalised its performance.

7.   Analysis and Discussion

The two parameters of study chosen among the dimensions of the damping rings are their cross-sectional area and their thickness. Finite-element (FE) simulations of high-strain-rate tension experiments are accomplished on Aluminum 7017-T73 alloy specimens when varying the thickness or the cross-sectional area of the damping rings.

All data shown below are relevant to the centre of the specimen (i.e., the area in which stresses and strains in the specimen reach their maximum values).

Figure 58 shows a comparison between the strain-time curves at the centre of the specimen for both the modified SHTB withoug the interruption device (Model-2) and the modified SHTB using 4-mm thick damping rings with a cross-sectional area of 364.4 mm^2 (Model-3)
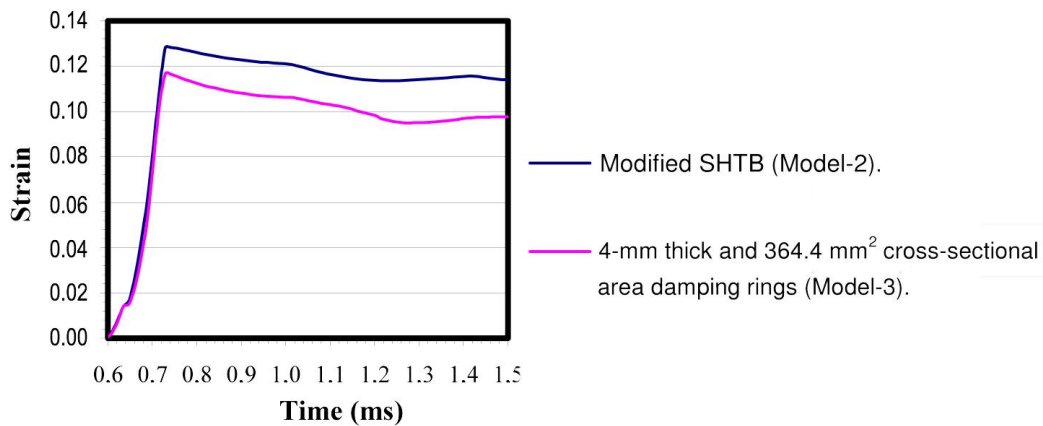

Figure 58. Strain in the centre of the specimen for both modified SHTB without interruption (Model-2) and modified SHTB using 4-mm thick and 364.4 mm^2 cross-section damping rings (Model-3).

Figure 59 shows that failure area is avoided (0.12) when the system is damped. The strain variation is shown as a function of the increase of the damping rings thickness when maintaining a cross-sectional area of 364.4 mm^2.
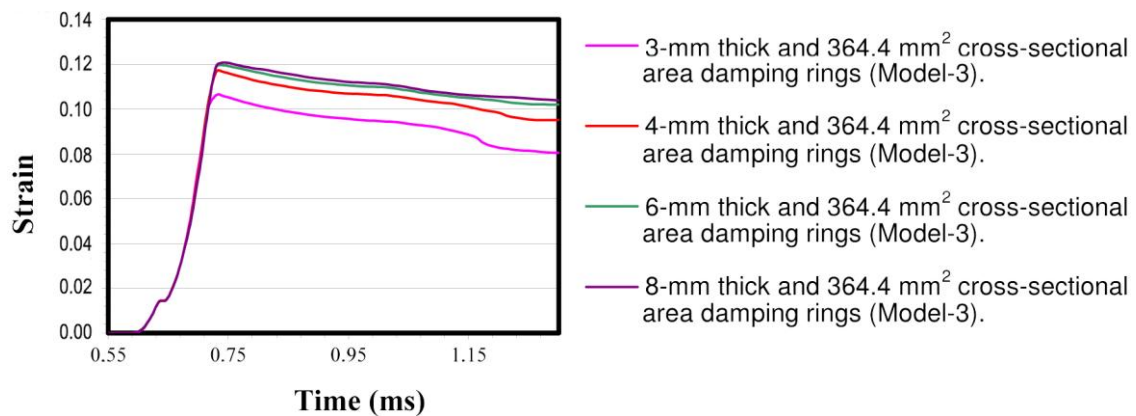

Figure 59. Strains in the centre of the specimen for a modified SHTB when using damping rings enclosed in an interruption fixture with different values of their thickness (Model-3).

Damping rings exceeding 4-mm thick cease offering a proper interruption effect. Therefore, thicknesses between 2 and 4 mm seem to be the most suitable for these experiments. However, these values only apply for damping rings made of lead and they do not apply to other materials. Figure 60 represents the maximum strain values as a function of the damping rings thickness. It also illustrates that the damping effect becomes significant when the damping rings thickness is under 4 mm. For values exceeding 4 mm, the strain tends asymptotically to the maximum strain value reached through the classical SHTB experiment (0.128).
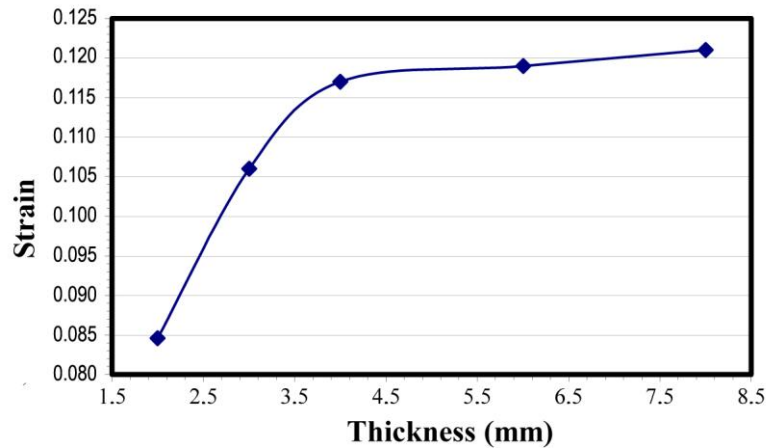
Figure 60. Strain in the centre of the specimen a function of the damping rings thickness.

Moreover, the influence of the cross-sectional area of the damping rings on the maximum strain of the specimen can also be analysed. The inner and outer diameters are both increased and decreased using a value of 0.5 mm each time yielding a range of cross-sectional areas that spans from 250 to 450 mm^2. Figures 61 and 63 show the comparison between the strains obtained in the specimen for the above-mentioned cross-sectional area range using 6-mm thick and 4-mm thick damping rings respectively.

Figure 61. Strain in the centre of the specimen as a function of the cross-sectional area of
6-mm thick damping rings.

Figure 60 shows that the influence of the cross-sectional area on the specimen strain is less significant than the above-mentioned influence of the damping rings thickness.
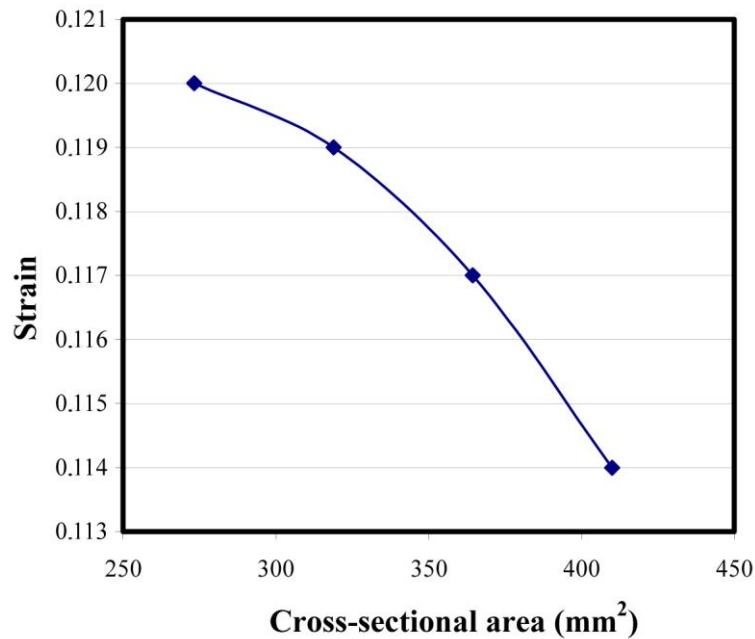
Figure 62. Strain in the centre of the specimen as a function of the cross-sectional area of 4-mm thick damping rings.

Figure 63 and figure 64 show the comparison between the strains obtained in the specimen for the above-mentioned cross-sectional area range using 3-mm thick and 4-mm thick damping rings respectively.
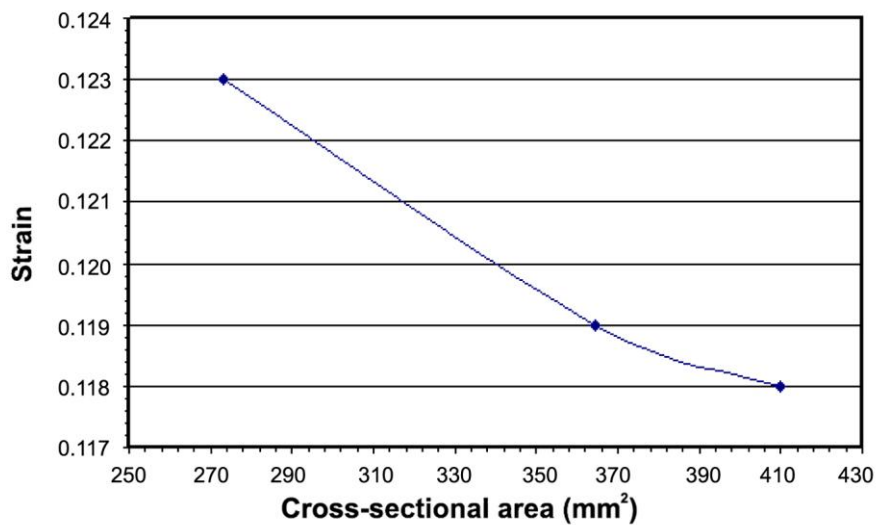

Figure 63. Strain in the centre of the specimen as a function of the cross-sectional area of 3-mm thick damping rings.

Considering that the difference of cross-sectional areas is lower than the one considered previously (increment of area = 91 mm^2), the difference of strains is however considerably greater (0.01) and therefore it can be demonstrated that the influence of the cross-sectional area of the damping rings on the strain values is less significant than the one relevant to its thickness.
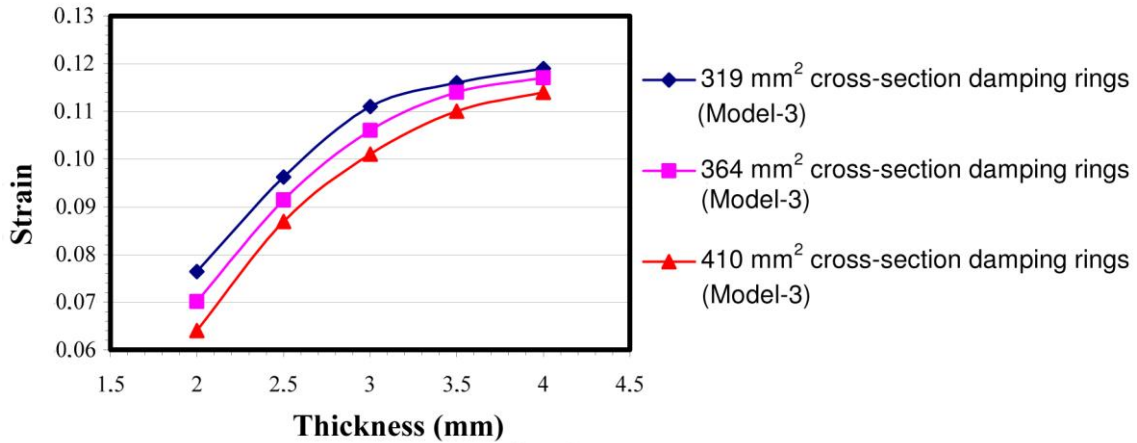
Figure 64. Strain in the centre of the specimen as a function of the damping rings thickness when considering different cross-sectional areas.

Damping rings with a thickness below 3 mm should be avoided in consideration of the reduction of the strain values obtained. Figure 65 clearly illustrates the influence of the cross-sectional area for each value of the damping rings thickness.
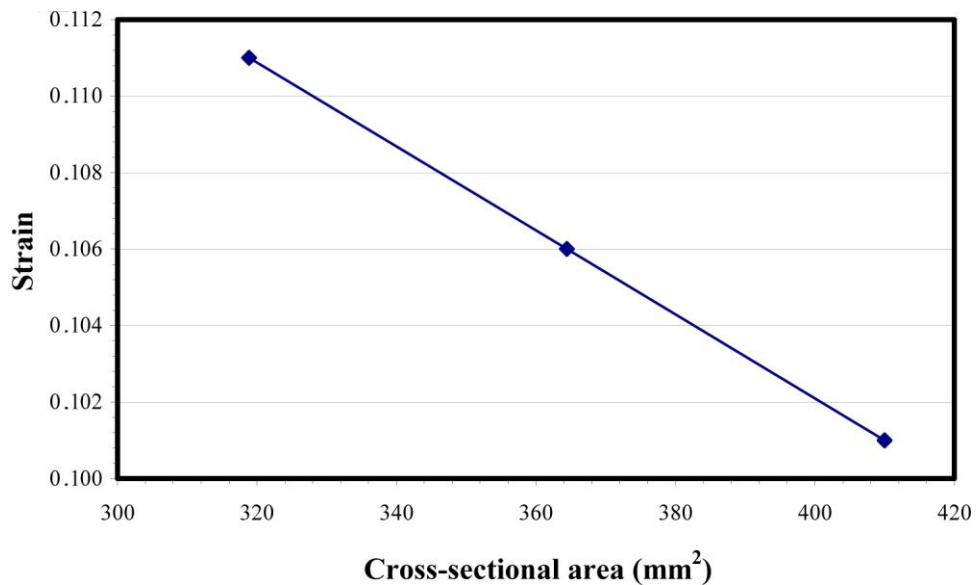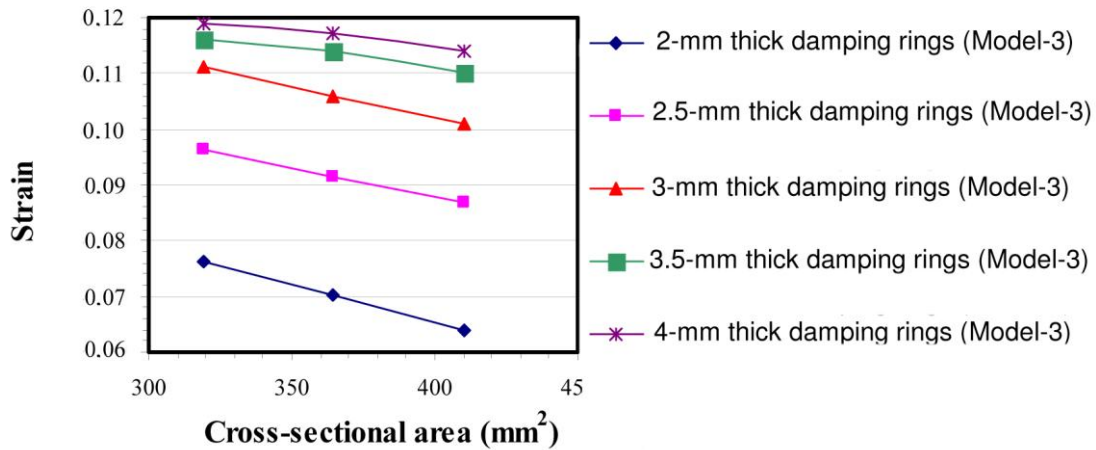

Figure 65. Strain in the centre of the specimen as a function of the cross-sectional area of the damping rings when varying their thickness.

The influence of the cross-sectional area increases along with the decrease of the thickness.

The main goal of this experiment is gathering information about the specimen's behaviour at high strain rates. Therefore, if the strain rate in the specimen decreases and high strain rates can not be maintained, the experiment must not be acceptable. Strain rate-time curves can be obtained in each case after finding the time derivative of the strain-time curves previously depicted.

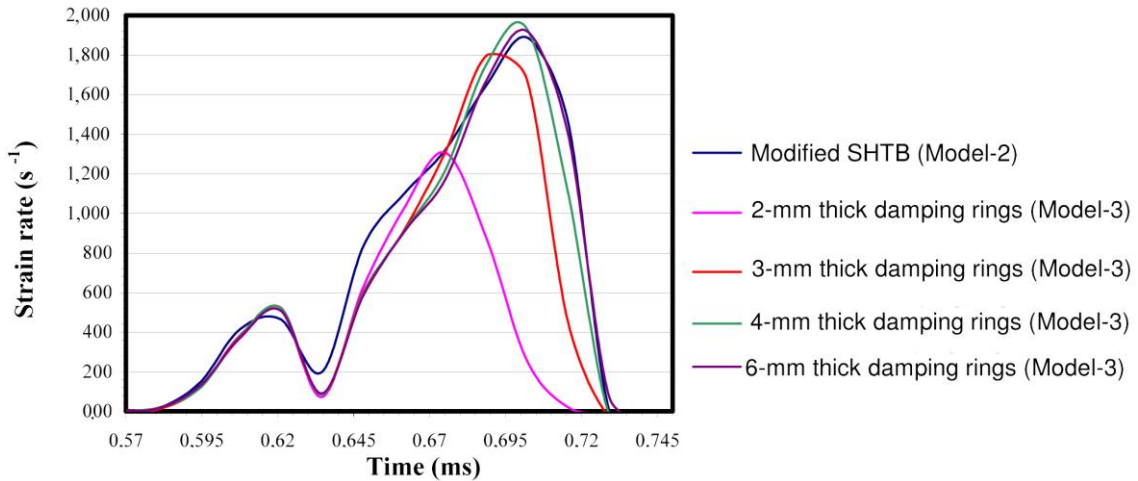*Figure 66. Strain rate in the centre of the specimen using different values of the damping rings thickness.*

Figure 66 shows that using 4-mm thick damping rings high strain rates can be obtained as desired. However, a thickness of 3 mm seems to be optimum for the study using lead as damping rings material, in view of the high strain rates reached in the specimen even when aluminum strain (around 0.1) does not exceed the strain relative to ultimate tensile strength (0.12), which is the main interest in such experiment.

In addition, 2-mm thick damping rings provide a substantial decrease of the maximum strain rate. Therefore, this value should also be excluded in order to pursue the experiment goal. The 3-mm thick damping rings are definitely the most suitable mechanism to accomplish the experiment on the Aluminum 7017-T73 alloy specimen when damping rings are made of lead.

Strain rate-time curves are depicted below when using 3-mm thick damping rings and different values of their cross-sectional areas. Non-interrupted SHTB (Model-2) results are also shown as a reference strain rate for comparison purposes.
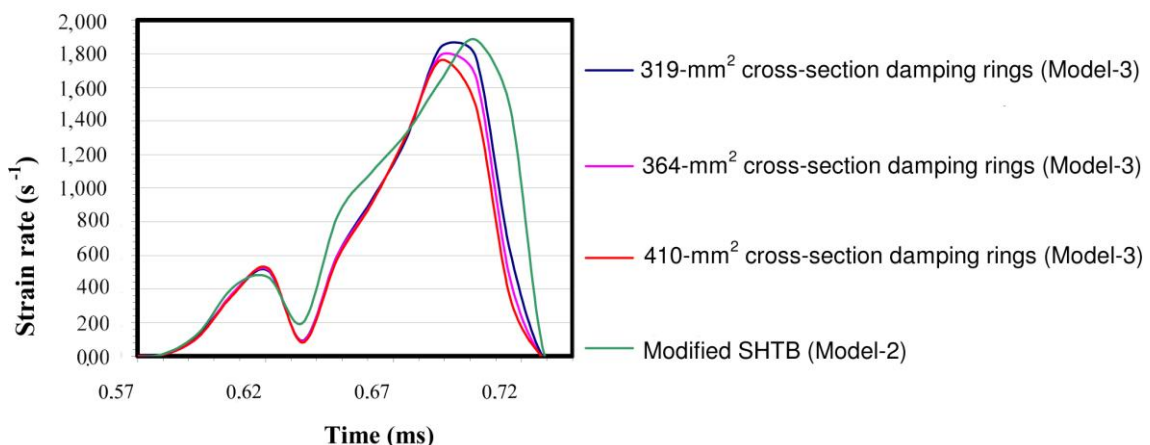

Figure 67. Strain rate in the centre of the specimen using different cross-sectional areas of the 3-mm thick damping rings.

As expected, a cross-sectional area of 319 mm^2 (i.e., the lowest one of all the cross-sectional areas considered) provides the maximum strain rate in the specimen. The strain rate variation must be definitely considered although it does not span a wide range.
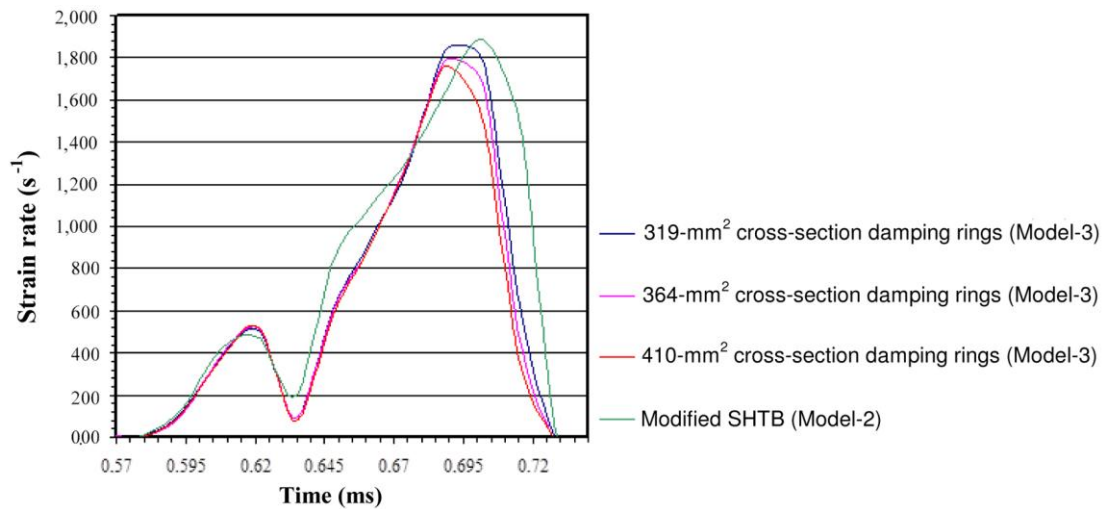

Figure 68. Strain rate in the centre of the specimen for different cross-sectional areas of the 3-mm thick damping ring.

Therefore, it can be concluded that the damping rings thickness definitely influences the values of both the strain and the strain rate in the specimen. FE analyses described herein are applied to simulate the effects of the variation of the damping rings dimensions to provide a reference for improvement of a modified SHTB experimental apparatus and guidance for future studies in which optimum dimensions for the damping rings can be studied.

8. Conclusions

A numerical analysis of the SHTB tests using an external interruption device has been carried out using FE method. The simulation results show that the designed interruption device has a significant effect on the obtained strain in the specimen. Experimental results with the modified SHTB using the interruption device confirmed the validity of the numerical analysis results and the capability of the developed interruption mechanism to stop the dynamic tensile tests at a predetermined elongation value. The elongation of the test specimen can be controlled by the length of the external interruption device.

Results of numerical simulations are presented of SHTB experiments considering different damping rings dimensions. The simulations provide complementary information to the experiments and in-depth understanding of the specimen behaviour.

The modified SHTB model when the cross-sectional area of the bar ends which are in contact with the specimen is increased (Model-2) is validated with the SHTB apparatus where high strain rate tensile experiments are made on Aluminum 7017-T73 alloy specimens. The differences between them are minimal and may therefore be neglected.

The modified SHTB model when using damping rings enclosed in the interruption device (Model-3) has been compared with the modified SHTB when the cross-sectional area of the bar ends which are in contact with the specimen is increased (Model-2). High strain rate tension

experiments are performed on Aluminum 7017-T73 alloy specimens using damping rings made of lead.

In this case the observed differences between them are significant and 1D stress wave propagation assumption becomes a challenging issue. However, when analysing the stress-strain conditions in both models, the stress in the specimen results diminished and failure is avoided, as expected, even when maintaining high-rate loading.

According to the strains and strain rates observed in the specimen, it has been numerically demonstrated that the cross-sectional area of the damping rings is not a relevant factor in the interruption process. Although an increment of the cross-sectional area of such damping rings results in an enhancement of the interruption process, such influence can be considered negligible when compared to the effect of the variation of the damping rings thickness.

Therefore, the cross-sectional area of the damping rings can be excluded as a factor influencing the results of the modified SHTB experiments and thickness can be considered the most significant parameter to influence the output results of the modified SHTB. The damping rings thickness results to be a significant parameter when dimensioning the interruption system. The 3-mm thick damping rings are definitely the most suitable mechanism to accomplish the experiment on the Aluminum 7017-T73 alloy specimen when damping rings are made of lead.

In view of this research, it can therefore be concluded that the thickness of the damping rings is a factor that can resolutely influence the interrupted dynamic tension experiment results whilst the influence of their volume and their cross-sectional area should not be considered as a factor influencing the results of the modified SHTB experiments. However, it should be emphasized that the validity of the conclusions is limited to the materials having a behaviour resembling the materials considered here.

9. Acknowledgements

10. References

[1] HARDING, J. & WELSH, L. 1983, "A Tensile Testing Technique for Fiber-Reinforced Composites at Impact Rates of Strain", *Journal of Materials Science,* vol. 18, no. 6, pp. 1810-1826.
[2] LINDHOLM, U. & YEAKLEY, L. 1968, "High Strain-Rate Testing - Tension and Compression", *Experimental Mechanics,* vol. 8, no. 1, pp. 1-&.
[3] ALBERTINI, C. & MONTAGNANI, M. 1976, "Wave-Propagation Effects in Dynamic Loading", *Nuclear Engineering and Design,* vol. 37, no. 1, pp. 115-124.

[4] NICHOLAS, T. 1981, "Tensile Testing of Materials at High-Rates of Strain", *Experimental Mechanics,* vol. 21, no. 5, pp. 177-185.

[5] STAAB, G. & GILAT, A. 1990, *A Direct Tension Split Hopkinson Bar for High-Strain Rate Testing,* SOC EXPERIMENTAL MECHANICS INC, BETHEL; BETHEL.

[6] Thakur, A., NematNasser, S. & Vecchio, K. 1996, "Dynamic Bauschinger effect", *Acta Materialia,* vol. 44, no. 7, pp. 2797-2807.

[7] Verleysen, P. & Degrieck, J. 2004, "Experimental investigation of the deformation of Hopkinson bar specimens", *International Journal of Impact Engineering,* vol. 30, no. 3, pp. 239-253.

[8] Gray, G.T. 2000, "Classic Split-Hopkinson Pressure Bar Testing.", *Materials Park, OH: ASM International, 2000.,* , pp. 462-476.

[9] Gama, B.A., Lopatnikov, S.L. & Gillespie, J.W. 2004, "Hopkinson bar experimental technique: a critical review", *Applied Mechanics Reviews,* vol. 57, no. 4, pp. 223-250.

[10] Gerlach, R., Kettenbeil, C. & Petrinic, N. 2012, "A new split Hopkinson tensile bar design", *International Journal of Impact Engineering,* vol. 50, pp. 63-67.

[11] Kolsky, H. 1949, "An Investigation of the Mechanical Properties of Materials at very High Rates of Loading", *Proceedings of the Physical Society.Section B,* vol. 62, no. 11, pp. 676.

[12] Rio, T., Barbero, E., Zaera, R. & Navarro, C. 2005, "Dynamic tensile behaviour at low temperature of CFRP using a split Hopkinson pressure bar", *Composites Science and Technology,* vol. 65, no. 1, pp. 61-71.

[13] Van Slycken, J. 2008, *Advanced Use of a Split Hopkinson Bar Setup-Application to TRIP Steels.*

[14] Hamouda, A. & Hashmi, M. 1998, "Testing of composite materials at high rates of strain: advances and challenges", *Journal of Materials Processing Technology,* vol. 77, no. 1-3, pp. 327-336.

[15] Gray, G.T. 2000, "Classic Split-Hopkinson Pressure Bar Testing.", *Materials Park, OH: ASM International, 2000.,* , pp. 462-476.

[16] Khlif, M., Masmoudi, N. & Bradai, C. 2012, "Polypropylene tensile test under quasi-static and dynamic loading", *Materials Science and Technology Conference and Exhibition 2012, MS and T 2012,* pp. 567.

[17] Verleysen, P., Benedict, V., Verstraete, T. & Joris, D. 2009, "Numerical study of the influence of the specimen geometry on split Hopkinson bar tensile test results", *Latin American Journal of Solids and Structures,* vol. 6, no. 3, pp. 285-298.

[18] Kaiser, M.A. 1998, *Advancements in the split Hopkinson bar test.*

[19] Swantek, S., Wicks, A. & Wilson, L. 2001, "An optical method of strain measurement in the split Hopkinson pressure bar", *Proceedings of Imac-Xix: a Conference on Structural Dynamics, Vols 1 and 2,* vol. 4359, pp. 1471-1477.

[20] Pérez-Martín, M.J., Erice, B. & Gálvez, F. 2014, "On the Loading-rate Dependence of the Al 7017-T73 Fracture-initiation Toughness", *Procedia Materials Science,* vol. 3, no. 0, pp. 1026-1031.

[21] Rodríguez Pérez, J. 2002, *Análisis y desarrollo de metodologías para la obtención de propiedades mecánicas de materiales a altas velocidades de deformación ya alta temperatura*.

[22] Resnyansky, A. 2000, "Study of influence of'loading method on results of the Split Hopkinson Bar test".

[23] Gerlach, R., Kettenbeil, C. & Petrinic, N. 2012, "A new split Hopkinson tensile bar design", *International Journal of Impact Engineering,* vol. 50, pp. 63-67.

[24] Yang, X., Xiong, X., Yin, Z., Wang, H., Wang, J. & Chen, D. 2014, "Interrupted Test of Advanced High Strength Steel with Tensile Split Hopkinson Bar Method", *Experimental Mechanics,* vol. 54, no. 4, pp. 641-652.

[25] NEMATNASSER, S., ISAACS, J. & STARRETT, J. 1991, "Hopkinson Techniques for Dynamic Recovery Experiments", *Proceedings of the Royal Society of London Series A-Mathematical Physical and Engineering Sciences,* vol. 435, no. 1894, pp. 371-391.

[26] Ma Dongfang, Chen Danian, Wu Shanxing, Wang Huanran, Hou Yanjun & Cai Canyuan 2010, "An interrupted tensile testing at high strain rates for pure copper bars", *Journal of Applied Physics,* vol. 108, no. 11, pp. 114902.

[27] Essa, Y.E., Lopez-Puente, J. & Perez-Castellanos, J.L. 2007, "Numerical simulation and experimental study of a mechanism for Hopkinson bar test interruption", *Journal of Strain Analysis for Engineering Design,* vol. 42, no. 3, pp. 163-172.

[28] Lezcano, R., Essa, Y. & Perez-Castellanos, J. 2003, "Numerical analysis of interruption process of dynamic tensile tests using a Hopkinson bar", *Journal De Physique Iv,* vol. 110, pp. 565-570.

[29] ASTM E8 / E8M-13a, Standard Test Methods for Tension Testing of Metallic Materials, ASTM International, West Conshohocken, PA, 2013, www.astm.org

[30] Rodríguez Pérez, J. 2002, *Análisis y desarrollo de metodologías para la obtención de propiedades mecánicas de materiales a altas velocidades de deformación ya alta temperatura*.

[31] Wu, X. & Gorham, D. 1997, "Stress equilibrium in the split Hopkinson pressure bar test", *Journal De Physique Iv,* vol. 7, no. C3, pp. 91-96.

[32] Jiang, F. & Vecchio, K.S. 2009, "Hopkinson Bar Loaded Fracture Experimental Technique: A Critical Review of Dynamic Fracture Toughness Tests", *Applied Mechanics Reviews,* vol. 62, no. 6, pp. 060802.

[33] ABAQUS, Version 5.8. Hibbit, Karlson and Sorensen, Inc., Pawtucket, RI

[34] Godunov, S.K. & Romenskii, E.I. 2003, *Elements of continuum mechanics and conservation laws,* Springer Science & Business Media.

[35] Essa, Y.E., Lopez-Puente, J. & Perez-Castellanos, J.L. 2007, "Numerical simulation and experimental study of a mechanism for Hopkinson bar test interruption", *Journal of Strain Analysis for Engineering Design,* vol. 42, no. 3, pp. 163-172.

11. About the authors

Roberto Alonso González Lezcano:

Doctorate in Industrial Engineering recognized by ACAP. Extraordinary Doctorate Award. Advanced degrees in Mechanical Engineering, Mathematics and Higher Education. Teacher in undergraduate and master programs in several areas such as: mechanical systems, electromechanics, materials, physics, mathematics, continuum mechanics and theory of structures in Polytechnic University (Madrid), European University (Madrid), Camilo José Cela University, Antonio de Nebrija University and Carlos III University (Madrid). Researcher in projects financed by public (CAM and CICYT) and private (EADS Airbus Defence & Space) entities. He currently is adjunct professor in San Pablo CEU University. Author of books and articles about mechanical systems and continuum mechanics.

José Manuel del Río Campos:

Doctorate in Industrial Engineering by the Polytechnic University of Madrid recognized by Quality, Accreditation and Prospective Agency (ACAP). M.S. in Science and Technology of Advanced Polymer-Based Materials by the Higher Scientific Research Centre (CSIC). He has taught in Carlos III University (Madrid) and in Antonio de Nebrija University (Madrid). His professional experience includes a post of Technical Assistant responsible for conducting the type-approval tests in ITSEMAP FUEGO (MAPFRE), Technician in Aid and Development in REPSOL YPF Materials Technology Center and Operator of crude in Trading Department. He currently is adjunct professor in San Pablo CEU University.